Cell Reports

Article

Multiple regulatory intrinsically disordered motifs control FOXO4 transcription factor binding and function

Graphical abstract

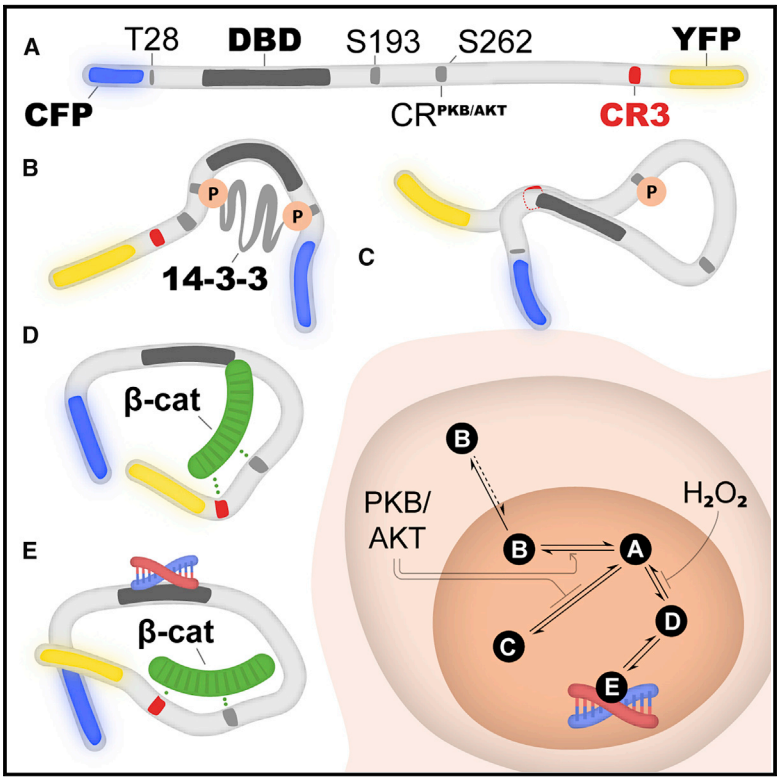

Highlights

- The interaction network between FOXO4 and β-catenin is deciphered
- FOXO4 autoinhibition interferes with DNA binding and is counteracted by β-catenin
- FOXO4 exists in multiple conformations regulated by phosphorylation and co-factors
- ICAT switches between FOXO4 and TCF/LEF transcription factors

Authors

Benjamin Bourgeois, Tianshu Gui, Diana Hoogeboom, ..., Klaus Richter, Tobias Madl, Boudewijn M.T. Burgering

Correspondence

tobias.madl@medunigraz.at (T.M.), b.m.t.burgering@umcutrecht.nl (B.M.T.B.)

In brief

Understanding the mechanistic base of transcription factor regulation is a prerequisite to understanding their (patho)physiology. Bourgeois et al. provide structural, biochemical, and *in vivo* analyses of the molecular mechanisms of FOXO4 binding and activation by β-catenin.

Bourgeois et al., 2021, Cell Reports *36*, 109446
July 27, 2021
https://doi.org/10.1016/j.celrep.2021.109446

CellPress

Cell Reports

CellPress
OPEN ACCESS

Article

Multiple regulatory intrinsically disordered motifs control FOXO4 transcription factor binding and function

Benjamin Bourgeois,[1,5] Tianshu Gui,[2,5] Diana Hoogeboom,[2,6] Henry G. Hocking,[3,7] Gesa Richter,[1] Emil Spreitzer,[1] Martin Viertler,[3,8] Klaus Richter,[3] Tobias Madl,[1,4,5,*] and Boudewijn M.T. Burgering[2,9,*]

[1]Gottfried Schatz Research Center for Cell Signaling, Metabolism and Aging, Molecular Biology and Biochemistry, Medical University of Graz, 8010 Graz, Austria

[2]Oncode Institute and Department of Molecular Cancer Research, Center for Molecular Medicine, University Medical Center Utrecht, 3584 CX Utrecht, the Netherlands

[3]Department Chemie, Technische Universität München, 85747 Garching, Germany

[4]BioTechMed-Graz, 8010 Graz, Austria

[5]These authors contributed equally

[6]Present address: Ausnutria B.V., 8025 BM Zwolle, the Netherlands

[7]Present address: Windfall Films, N1 7LZ London, UK

[8]Present address: Novartis, Global Drug Development, Technical Research and Development, 6336 Langkampfen, Austria

[9]Lead contact

*Correspondence: tobias.madl@medunigraz.at (T.M.), b.m.t.burgering@umcutrecht.nl (B.M.T.B.)

https://doi.org/10.1016/j.celrep.2021.109446

SUMMARY

Transcription factors harbor defined regulatory intrinsically disordered regions (IDRs), which raises the question of how they mediate binding to structured co-regulators and modulate their activity. Here, we present a detailed molecular regulatory mechanism of Forkhead box O4 (FOXO4) by the structured transcriptional co-regulator β-catenin. We find that the disordered FOXO4 C-terminal region, which contains its transactivation domain, binds β-catenin through two defined interaction sites, and this is regulated by combined PKB/AKT- and CK1-mediated phosphorylation. Binding of β-catenin competes with the autoinhibitory interaction of the FOXO4 disordered region with its DNA-binding Forkhead domain, and thereby enhances FOXO4 transcriptional activity. Furthermore, we show that binding of the β-catenin inhibitor protein ICAT is compatible with FOXO4 binding to β-catenin, suggesting that ICAT acts as a molecular switch between anti-proliferative FOXO and pro-proliferative Wnt/TCF/LEF signaling. These data illustrate how the interplay of IDRs, post-translational modifications, and co-factor binding contribute to transcription factor function.

INTRODUCTION

Transcription factors (TFs) often contain intrinsically disordered regions (IDRs) that can play unique roles in transcription, for example, through mediating distinct patterns of interactions (Dyson and Wright, 2005; Habchi et al., 2014; Theillet et al., 2014; Tompa, 2012; Uversky et al., 2014; van der Lee et al., 2014; Wright and Dyson, 2015). Examples are liquid-liquid phase separation (Boija et al., 2018; Sabari et al., 2018), DNA-search (Vuzman et al., 2010), and DNA binding site selection (Brodsky et al., 2020; Guo et al., 2012). A common feature of these examples is that the involved IDRs mediate a network of weak multivalent interactions among one another as well as with folded co-factors and DNA. Due to their critical biological importance, these interaction patterns are tightly regulated by post-translational modifications (PTMs) and alternative splicing (Bah and Forman-Kay, 2016; Theillet et al., 2014; Wright and Dyson, 2015). *In vivo*, this enables fine-tuning of specific binding to their target promoters via TF subcellular localization, DNA binding, and transcription (trans)-activation (Inukai et al., 2017; Lambert et al., 2018). However, experimental evidence supporting the contribution of multivalent interactions and PTMs of TF IDRs to *in vitro* and *in vivo* binding of co-factors is not yet available.

To examine for a possible role of IDRs in co-factor binding via multivalent interactions and PTMs, we focused on Forkhead Box O4 (FOXO4) and the transcriptional regulator β-catenin. FOXO4 is a member of the FOX family of TFs, containing >50 members classified in 19 subgroups (FOXA to FOXS) (Hannenhalli and Kaestner, 2009; Lam et al., 2013). FOX proteins are evolutionarily highly conserved and play key roles in developmental and homeostatic processes, including cell-cycle control, cell differentiation, and proliferation (Klotz et al., 2015; van der Horst and Burgering, 2007). Within the FOX family, FOXOs are a class of TFs that contain largely unstructured N- and C-terminal regions flanking a central structured Forkhead (FH) domain that mediates sequence-specific DNA binding (Boura et al., 2010; Brent et al., 2008; Tsai et al., 2007; Weigel and Jäckle, 1990). FOXOs are regulated through growth factor signaling by the

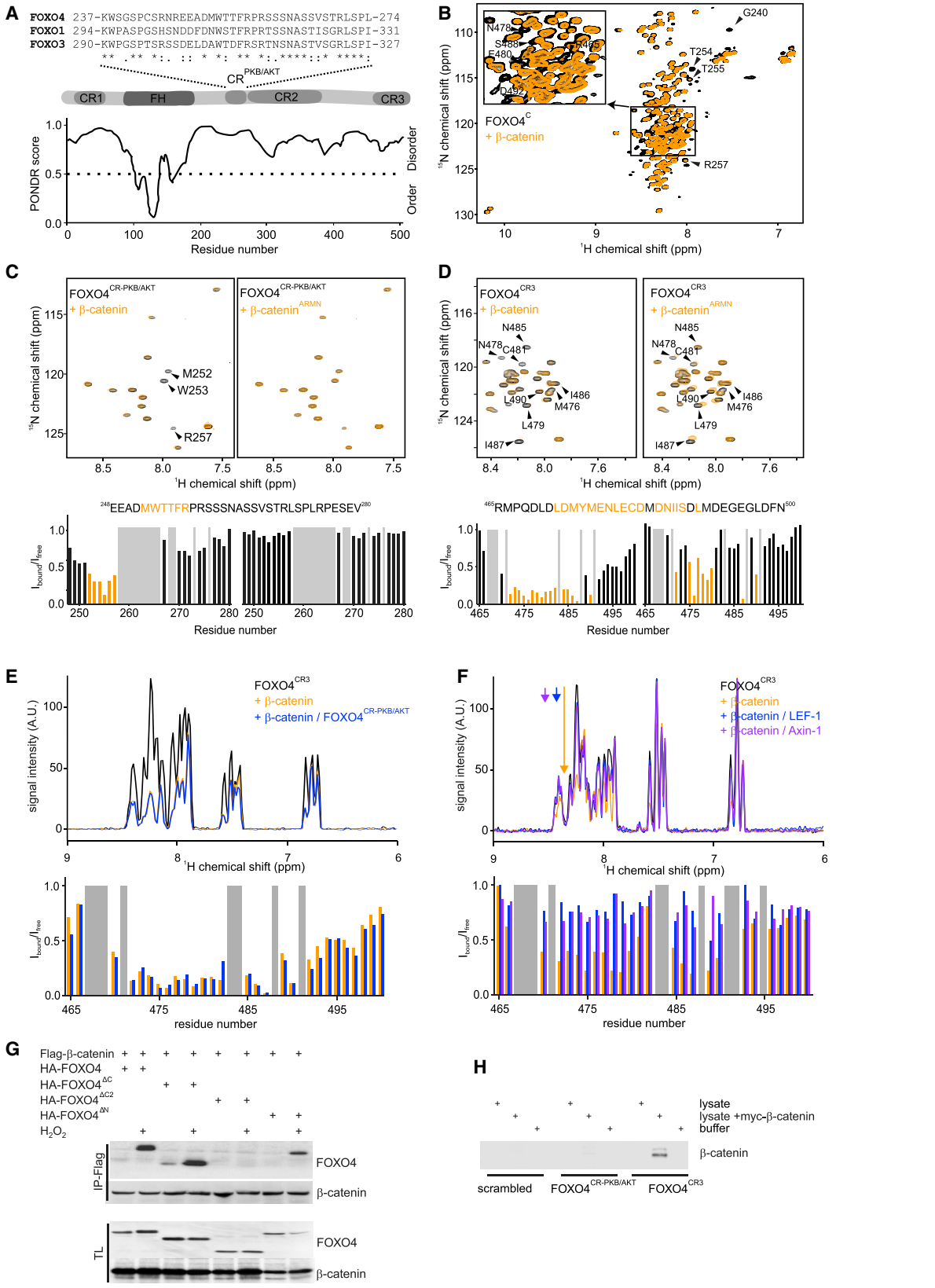

(legend on next page)

phosphoinositide 3-kinase (PI3K) pathway and by changes in the cellular redox state often referred to as oxidative stress-mediated signaling (Burgering and Medema, 2003; Essers et al., 2004; Klotz et al., 2015; Manning and Toker, 2017; van der Horst and Burgering, 2007). FOXOs are involved in a variety of cellular responses and biological processes, like cell-cycle and cell survival, metabolism and redox regulation, and DNA repair and differentiation (Eijkelenboom and Burgering, 2013). Importantly, in model systems, FOXO activity is associated with lifespan (Davy et al., 2018). FOXO regulation involves binding of many different co-factors, and the binding of these co-factors is regulated through various PTMs, including phosphorylation, methylation, acetylation, and ubiquitination (Eijkelenboom and Burgering, 2013).

The transcriptional co-factor β-catenin is one of the described FOXO binding partners. Like FOXOs, β-catenin is a multifunctional protein involved in cell adhesion and proliferation (Clevers and Nusse, 2012; MacDonald et al., 2009; Valenta et al., 2012). Increased cellular oxidative stress promotes the association of FOXOs with β-catenin, thereby enhancing FOXO transcriptional activity (Essers et al., 2005). Binding of β-catenin to FOXO inversely correlates with Wnt/TCF/LEF-mediated transcription, and this shift of β-catenin from TCF to FOXO has been shown to play a role in colon cancer metastasis (Tenbaum et al., 2012), osteoblast differentiation (Almeida et al., 2007), liver metabolism (Liu et al., 2011), and kidney fibrosis (Rao et al., 2019). Furthermore, Wnt/TCF/LEF signaling is shown to regulate FOXO1 nuclear exclusion in mammary stem cells through AKT (Sreekumar et al., 2017), and β-catenin regulation by PI3K signaling, possibly through GSK3, has been shown in many studies, but remains debated (Ng et al., 2009). Despite the importance of the interplay between these two major signaling pathways (Wnt/TCF/LEF and PI3K) at the level of FOXOs and β-catenin, the mechanism as to how β-catenin binds FOXOs and how this may regulate transcriptional activity remains unknown.

At least three FOXO isoforms, FOXO1, FOXO3, and FOXO4, interact with β-catenin (Essers et al., 2005; Hoogeboom et al., 2008). Here, we chose to study β-catenin binding to FOXO4 as a representative example of how a key co-factor binds to the IDR of FOXOs, how this is regulated by phosphorylation, and how this ultimately affects DNA binding and transcriptional activity. We present structural, biochemical, and *in vivo* analyses of the molecular mechanisms of FOXO4 binding and activation by β-catenin.

RESULTS

β-catenin binds multiple sites on FOXO4 involving the FH domain and the intrinsically disordered C terminus

Human FOXO4 is composed of a short N-terminal disordered region (residues 1–85) followed by a folded DNA binding domain, the FH domain (residues 91–188) and a long, disordered, C-terminal region (residues 189–505) (Bourgeois and Madl, 2018; Hartlmüller et al., 2019). Among the FOXO proteins, three disordered regions localized within the N and C termini have been reported to be conserved and called CR1 (residues 16–40 in FOXO4), CR2 (residues 278–374 in FOXO4), and CR3 (469–503 in FOXO4), respectively (Wang et al., 2012) (Figure 1A). In addition, FOXO1, FOXO3, and FOXO4 contain a conserved region N-terminal of CR2, which we call $CR^{PKB/AKT}$ (Figure 1A).

To map the precise binding site of β-catenin on FOXO4, we used purified proteins and NMR spectroscopy. We studied the binding of β-catenin to (1) the entire region N-terminal of the FH domain ($FOXO4^{N}$), (2) the FH domain ($FOXO4^{FH}$), and (3) the entire region C-terminal of the FH domain comprising the trans-activation domain ($FOXO4^{C}$). The ^{1}H, ^{15}N chemical shifts of ^{15}N-labeled $FOXO4^{N}$ and $FOXO4^{C}$ are in regions that are characteristic of a random coil protein, which show that in solution, the N- and C-terminal regions of FOXO4 are disordered (Figures S1A and S1B, respectively). The addition of unlabeled β-catenin to a solution of ^{15}N-labeled $FOXO4^{N}$ had no effect on the ^{1}H, ^{15}N heteronuclear single quantum coherence (HSQC) spectrum, showing that the N-terminal region of FOXO4 is not involved in β-catenin binding (Figure S1A). In contrast, the binding of β-catenin to $FOXO4^{C}$ and $FOXO4^{FH}$ was detected as shown by a decrease in signal intensity of several FOXO4 ^{1}H, ^{15}N HSQC cross-peaks upon the addition of unlabeled β-catenin (Figures 1B and S1B,

Figure 1. β-catenin binds multiple sites within FOXO4

(A) Positions of the FOXO conserved disordered regions (CR1, CR2, CR-PKB/AKT, and CR3) and the FH domain are indicated. Clustal-omega-based sequence alignment of the FOXO1, FOXO3, and FOXO4 CR-PKB/AKT region is shown (Madeira et al., 2019), as well as the PONDR score of human FOXO4 using the VSL2 predictor (http://www.pondr.com).

(B) ^{1}H, ^{15}N HSQC spectrum of ^{15}N-labeled $FOXO4^{C}$ at 100 μM with (orange) or without (black) addition of 1 equiv β-catenin. Residues corresponding to non-overlapping ^{1}H, ^{15}N cross-peaks and affected upon β-catenin binding are indicated in black.

(C) ^{1}H, ^{15}N HSQC spectrum of ^{15}N-labeled $FOXO4^{CR\text{-}PKB/AKT}$ at 50 μM with (orange) or without (black) addition of 1 equiv β-catenin (left panel) or $β\text{-catenin}^{ARMN}$ (right panel).

(D) ^{1}H, ^{15}N HSQC spectrum of ^{15}N-labeled $FOXO4^{CR3}$ at 50 μM with (orange) or without (black) addition of 1 equiv β-catenin (left panel) or $β\text{-catenin}^{ARMN}$ (right panel).

(E) Overlay of the ^{1}H projection of the ^{1}H, ^{15}N HSQC spectrum of free ^{15}N-labeled $FOXO4^{CR3}$ or in the presence of 1 equiv β-catenin or 5:1 equiv $FOXO4^{CR\text{-}PKB/AKT}$/β-catenin (black, orange, and blue lines, respectively).

(F) Overlay of the ^{1}H projection of the ^{1}H, ^{15}N HSQC spectrum of free ^{15}N-labeled $FOXO4^{CR3}$ or in the presence of 1 equiv β-catenin or 1:1 equiv LEF-1/β-catenin or 1:1 equiv Axin-1/β-catenin (black, orange, blue, and green lines, respectively).

(G) HEK293T cells were transfected with FLAG-β-catenin and HA-FOXO4 full-length or indicated deletion mutants, namely −ΔC(aa 1–415), −ΔC2(aa 1–266), and −ΔN(aa 193–505). Cells were treated with 100 μM H_2O_2 for 1 h, as indicated. Lysates were immunoprecipitated with anti-FLAG beads, followed by immunoblotting with anti-HA and anti-FLAG antibodies.

(H) HEK293T cells were transfected with myc-β-catenin and lysates were added to biotin-labeled $FOXO4^{CR\text{-}PKB/AKT}$ (aa 240–280) or $FOXO4^{CR3}$ (aa 464–505) peptides. Peptides were pulled down with streptavidin beads followed by immunoblotting with anti-myc antibody.

See also Figure S1.

respectively). The mapping of FOXO4 FH amino acids (aa) involved in β-catenin interaction was impossible as all FOXO4^{FH} ^{1}H,^{15}N HSQC cross-peaks completely disappeared upon binding (Figure S1B). In the case of FOXO^{C}, we observed the disappearance of several ^{1}H, ^{15}N HSQC cross-peaks upon the addition of β-catenin corresponding to residues clustered in two distinct regions: (1) residues Gly240, Thr254, Thr255, and Arg257 located within CR$^{PKB/AKT}$ and (2) residues Arg465, Asn478, Glu480, Ser488, and Asp492 located within CR3 (Figure 1B).

To determine whether CR$^{PKB/AKT}$ and CR3 are sufficient for β-catenin binding and to resolve the NMR signal overlap of the 317 residues-long FOXO4^{C}, we examined the binding of CR$^{PKB/AKT}$ and CR3 regions separately using NMR spectroscopy and fluorescence anisotropy. In line with the results obtained for FOXO4^{C}, β-catenin binds to both FOXO4$^{CR\text{-}PKB/AKT}$ and FOXO4^{CR3}, as shown by the disappearance of FOXO4 ^{1}H, ^{15}N HSQC cross-peaks upon the addition of unlabeled β-catenin (Figures 1C and 1D, respectively). Close inspection of the affected FOXO4 ^{1}H, ^{15}N HSQC cross-peaks revealed that the region from residues 252–257 (FOXO4$^{CR\text{-}PKB/AKT}$; Figure 1C, left panel) and 475–487 (FOXO4^{CR3}; Figure 1D, left panel) are mainly involved in β-catenin interaction. Given that the ^{1}H, ^{15}N HSQC cross-peaks corresponding to FOXO4$^{CR\text{-}PKB/AKT}$ residues 258–266 are invisible at the applied pH, we cannot exclude their involvement in β-catenin binding. In conclusion, the CR$^{PKB/AKT}$ and CR3 of the C-terminal FOXO4 IDR harboring the transactivation domain can interact with β-catenin independently.

Next, we wanted to assess whether the three β-catenin binding sites of FOXO4, the FH domain, CR$^{PKB/AKT}$, and CR3, overlap on β-catenin or allow simultaneous binding. β-Catenin is composed of a central folded Armadillo repeat region and flexible N and C termini. Although the Armadillo repeat region on its own could not be used due to aggregation, we managed to purify a β-catenin construct containing the first four repeats of the folded Armadillo repeat region (β-catenin^{ARMN}) (de la Roche et al., 2012). The addition of unlabeled β-catenin^{ARMN} to a solution of isotope-labeled FOXO4^{N}, FOXO4^{FH}, and FOXO4$^{CR\text{-}PKB/AKT}$ had no detectable effect on the associated ^{1}H, ^{15}N HSQC spectra, showing that these FOXO4 regions were not involved in β-catenin^{ARMN} binding (Figures 1C, right panel, S1A, right panel, and S1C). In contrast, β-catenin^{ARMN} binds to FOXO4^{CR3}, as shown by chemical shift perturbations (CSPs) of a subset of FOXO4 ^{1}H, ^{15}N HSQC cross-peaks upon the addition of unlabeled β-catenin^{ARMN} (Figure 1D, right panel). Close inspection of the affected FOXO4 ^{1}H, ^{15}N HSQC cross-peaks revealed that the same FOXO4^{CR3} residues are involved than when titrated with full-length β-catenin (Figure 1D). Similarly, the addition of unlabeled FOXO4^{CR3} to a solution of isotope-labeled β-catenin^{ARMN} led to progressive CSPs of a subset of β-catenin^{ARMN} ^{1}H, ^{15}N HSQC cross-peaks (Figure S1E, left panel), whereas no change was detected upon the addition of FOXO4$^{CR\text{-}PKB/AKT}$ (Figure S1E, right panel), confirming binding between the FOXO4 CR3 but not CR$^{PKB/AKT}$ and the N-terminal half of the Armadillo repeat region of β-catenin. In agreement, the addition of an excess of unlabeled FOXO4$^{CR\text{-}PBK/AKT}$ does not compete off ^{15}N-labeled FOXO4^{CR3} from β-catenin, as indicated by similar ^{1}H, ^{15}N HSQC projections of β-catenin-bound CR3 in presence or absence of CR$^{PKB/AKT}$ as well as associated intensity ratio plot of the FOXO4^{CR3} ^{1}H, ^{15}N HSQC cross-peaks (Figure 1E). Conversely, the addition of an equimolar amount of unlabeled LEF-1 or Axin-1 does compete off ^{15}N-labeled FOXO4^{CR3} from β-catenin, as indicated by CR3 signal recovery in the ^{1}H, ^{15}N HSQC projection, as well as the associated intensity ratio plot of the FOXO4^{CR3} ^{1}H, ^{15}N HSQC cross-peaks (Figure 1F). Thus, Axin-1/LEF-1 and FOXO4 compete for β-catenin binding. This is in line with the reported three-dimensional (3D) structures of β-catenin bound to LEF-1 and Axin-1 (PDB: 3OUW and PDB: 1QZ7, respectively; Sun and Weis, 2011; Xing et al., 2003), showing that both LEF-1 and Axin-1 bind to the first four repeats of the folded Armadillo repeat region.

To determine the contribution of the different FOXO4 regions to β-catenin binding *in vivo*, we analyzed binding by co-immunoprecipitation. Full-length FOXO4 co-precipitates with β-catenin, and binding was increased following H_2O_2 treatment (Figure 1G). In agreement with the NMR data, deletion only of the N-terminal disordered region of FOXO4 (HA-FOXO4$^{\Delta N}$) or deletion only of the CR3 (HA-FOXO4$^{\Delta C}$) did not result in the loss of β-catenin binding (Figure 1G). Co-deletion of the CR3 and part of the CR$^{PKB/AKT}$ (HA-FOXO4$^{\Delta C2}$) abrogates β-catenin binding to FOXO4, showing that both binding sites are necessary (Figure 1G). Moreover, this shows that the FH domain on its own is insufficient for β-catenin binding in cell-based assays. Second, to test whether the CR$^{PKB/AKT}$ and the CR3 on their own are sufficient for β-catenin binding, we tested β-catenin binding to biotin-tagged FOXO4$^{CR\text{-}PKB/AKT}$ and FOXO4^{CR3} peptides. Binding of β-catenin was observed for FOXO4^{CR3} and to a lower extent for FOXO4$^{CR\text{-}PKB/AKT}$ (Figure 1H).

AKT/CK1-mediated phosphorylation of FOXO4 CR$^{PKB/AKT}$ inhibits β-catenin binding

We and others have shown that several serine residues within or close to FOXO CR$^{PKB/AKT}$ can become phosphorylated (Biggs et al., 1999; Brunet et al., 1999; de Keizer et al., 2010; Kops et al., 1999; Rena et al., 1999; https://www.phoshosite.org). We hypothesized that phosphorylation of the CR$^{PKB/AKT}$ regulates β-catenin binding to FOXO4.

Therefore, we examined the phosphorylation status of the FOXO4 CR$^{PKB/AKT}$ using NMR-based phosphorylation assays in human cell lysate and with recombinant human AKT and CK1 kinases, respectively. NMR spectroscopy is well suited to site-specific mapping of protein phosphorylation reactions in IDRs and allows one to distinguish multiple phosphorylation events at closely spaced or adjacent substrate sites (Theillet et al., 2013). Incubation of a solution of isotope-labeled FOXO4$^{CR\text{-}PKB/AKT}$ in human HEK293T cell lysate led to the disappearance of ^{1}H, ^{15}N HSQC cross-peaks of serine residues together with the re-appearance of NMR cross-peaks within a region characteristic for phosphorylated serines and threonines (Figure 2A). The identities of the phosphorylated residues were unambiguously assigned to Ser241, Ser262, Ser265, and Ser268 through kinases endogenously present in HEK293T cell lysate, and no additional phosphorylation events occurred. Ser241 has been previously reported to be phosphorylated by c-Jun N-terminal kinase and has not been further evaluated here (de Keizer et al., 2010). To test whether AKT is sufficient for mediating the phosphorylation of Ser262 and subsequently CK1 for Ser265 and Ser268, we incubated a solution of

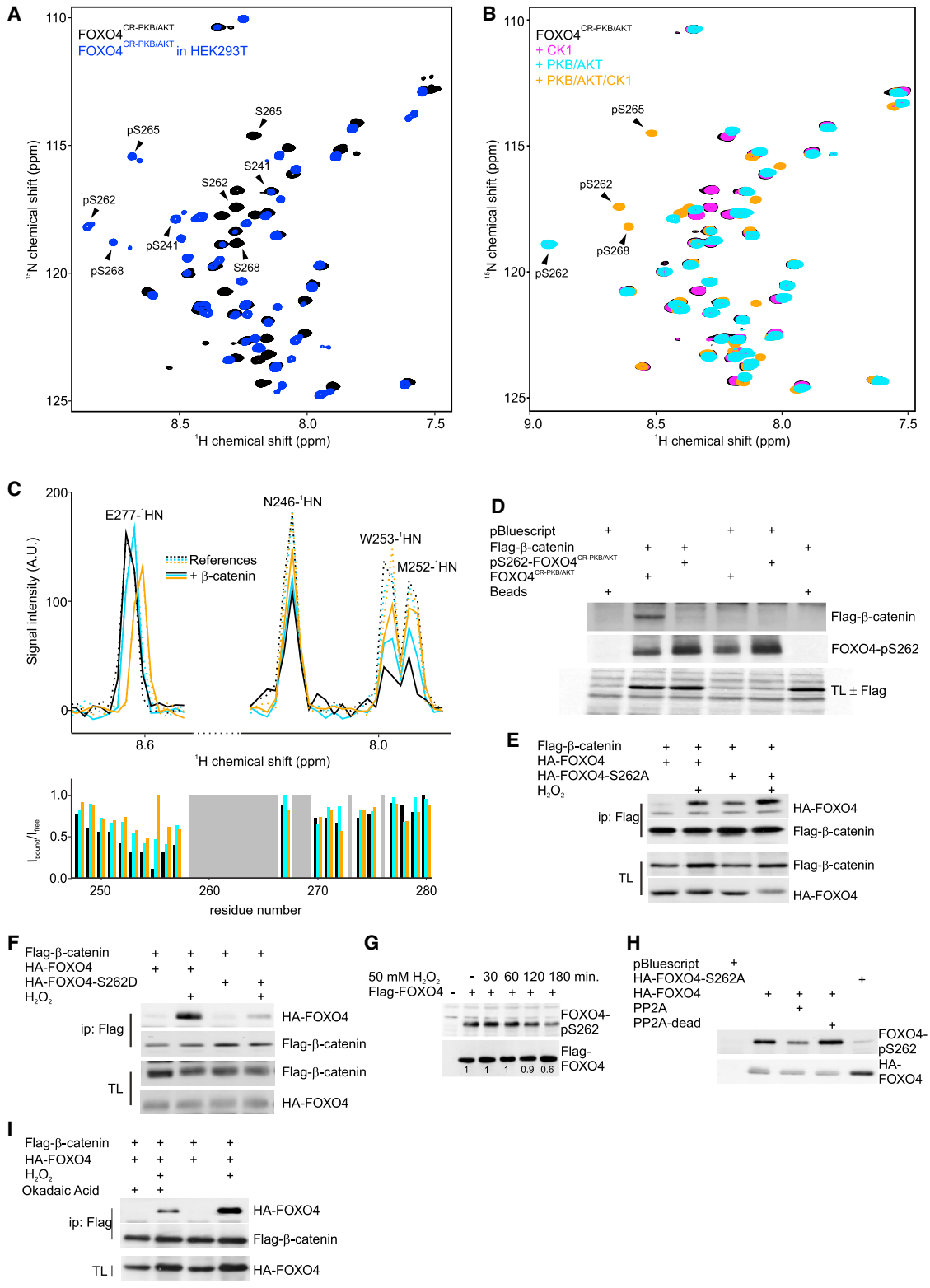

Figure 2. PKB/casein kinase I (CKI)-mediated phosphorylation of the FOXO4$^{CR\text{-}PKB/AKT}$ region regulates FOXO4/β-catenin interaction

(A) ^{1}H, ^{15}N HSQC spectrum of ^{15}N-labeled FOXO4$^{CR\text{-}PKB/AKT}$ at 50 μM with (blue) or without (black) overnight incubation in human HEK293T cell lysate. The ^{1}H, ^{15}N HSQC cross-peaks corresponding to the phosphorylated and non-phosphorylated forms of the S241, S262, S265, and S268 are indicated in black.

(legend continued on next page)

^{13}C,^{15}N-labeled $FOXO4^{CR\text{-}PKB/AKT}$ with either recombinant PKB/AKT alone, CK1 alone, or AKT together with CK1. AKT addition to a solution of ^{15}N-labeled $FOXO4^{CR\text{-}PKB/AKT}$ led to the disappearance of a ^{1}H, ^{15}N HSQC cross-peak corresponding to Ser262 and the re-appearance of a ^{1}H-^{15}N HSQC cross-peak in a region characteristic for phosphorylated serines (Figure 2B, cyan spectra). In contrast, the addition of CK1 did not show any phosphorylation (Figure 2B; magenta spectra), whereas the addition of AKT together with CK1 resulted in the phosphorylation of Ser262, Ser265, and Ser268 (Figure 2B, orange spectra). All of the phosphorylation events were unambiguously assigned. These data show that AKT is sufficient for mediating the phosphorylation of $FOXO4^{CR\text{-}PKB/AKT}$ Ser262 and acts as a priming phosphorylation event allowing the CK1-mediated phosphorylation of Ser265 and Ser268.

Given that we detected $FOXO4^{CR\text{-}PKB/AKT}$ phosphorylation *in vitro*, we studied the impact of phosphorylation on β-catenin binding. To this end, we tested the binding of β-catenin to different $FOXO4^{CR\text{-}PKB/AKT}$ versions using NMR spectroscopy, including (1) un-phosphorylated, (2) AKT-phosphorylated, and (3) AKT-CK1-phosphorylated $FOXO4^{CR\text{-}PKB/AKT}$. To visualize the differential binding of $FOXO4^{CR\text{-}PKB/AKT}$ versions upon the addition of β-catenin, we analyzed projections of the ^{1}H, ^{15}N HSQC as well as the associated intensity ratio plot of the $FOXO4^{CR\text{-}PKB/AKT}$ ^{1}H, ^{15}N HSQC cross-peaks. The addition of β-catenin to a solution of ^{15}N-labeled $FOXO4^{CR\text{-}PKB/AKT}$ leads to a decrease in signal intensity of ^{1}H, ^{15}N HSQC cross-peaks (Figure 1C) and of their associated ^{1}H projection corresponding to $FOXO4^{CR\text{-}PKB/AKT}$ residues 252 and 253 (Figure 2C, black solid and dotted lines). In contrast, the addition of β-catenin to a solution of either AKT-phosphorylated or AKT/CK1-phosphorylated ^{15}N-labeled $FOXO4^{CR\text{-}PKB/AKT}$ resulted in a lower reduction of signal intensity compared to un-phosphorylated ^{15}N-labeled $FOXO4^{CR\text{-}PKB/AKT}$ (Figure 2C, cyan and orange, respectively, solid and dotted lines). We also observed a correlation between a higher degree of phosphorylation (1 or 3 phosphorylation events for AKT or AKT/CK1, respectively) and a lower reduction in signal intensity of the 252 and 253 ^{1}H, ^{15}N HSQC cross-peaks of $FOXO4^{CR\text{-}PKB/AKT}$ upon β-catenin binding.

Next, we aimed to confirm the reduced β-catenin binding of phosphorylated $FOXO4^{CR\text{-}PKB/AKT}$ *in vivo*. As shown, exogenously expressed β-catenin can be efficiently pulled down by a synthetic biotin-tagged $FOXO4^{CR\text{-}PKB/AKT}$ peptide, but importantly, the synthetic Ser262 phosphorylated $CR^{PKB/AKT}$ peptide lost its ability to bind to exogenous β-catenin (Figure 2D). In agreement, we observed that the mutation of FOXO4 Ser262 to alanine (S262A), mimicking the loss of phosphorylation, resulted in a consistent increase in basal and H_2O_2-induced interaction between transiently expressed β-catenin and FOXO4, whereas a phospho-mimicking mutant of FOXO4 (S262D) had the opposite effect (Figures 2E and 2F, respectively). This is in agreement with our NMR data, showing that phosphorylation of the FOXO4 $CR^{PKB/AKT}$, including Ser262, weakens the binding of FOXO4 to β-catenin (Figure 2C). Importantly, we observed that H_2O_2 treatment resulted in a progressive decrease in FOXO4 phosphorylation at the Ser262 site over time (Figure 2G), suggesting that redox stress increases β-catenin binding to FOXO4 at least in part through Ser262 dephosphorylation.

Several phosphatases have been claimed to de-phosphorylate FOXOs, including PP2A (Singh et al., 2010). We therefore tested whether PP2A is involved in de-phosphorylation of the FOXO4 Ser262 site and subsequently regulates FOXO4 binding to β-catenin in cells. We observed that incubation of FOXO4 with recombinant active, not inactive, PP2A resulted in decreased Ser262 phosphorylation (Figure 2H). In agreement, we observed an increased pull-down of transiently expressed FOXO4 to β-catenin in cells treated with okadaic acid, a generic PP2A phosphatase inhibitor (Figure 2I).

FOXO4 adopts an autoinhibited conformation, which weakens its affinity for DNA

Previous studies demonstrated that the CR3 within the FOXO3a C-terminal disordered region interacts *in cis* with the FOXO3a FH domain on a surface that overlaps with its DNA binding site (Wang et al., 2008). As the aa sequence of FOXO3a CR3 is highly conserved in FOXO4 (Figure 1A), we hypothesized that the FOXO4 C-terminal disordered region can interact as well with the FH domain, thus inhibiting DNA binding.

To validate our hypothesis, we examined the 3D conformation of FOXO4 in the absence of DNA. Although full-length FOXO4 could not be obtained due to proteolytic degradation, we succeeded in purifying a shorter construct harboring the FH domain

(B) ^{1}H, ^{15}N HSQC spectrum of ^{15}N-labeled $FOXO4^{CR\text{-}PKB/AKT}$ at 50 μM without (black) or with incubation of recombinant CKI at 12 nM (magenta), AKT at 7 nM (cyan), and CKI plus AKT at 12 and 7 nM, respectively (orange). The ^{1}H, ^{15}N HSQC cross-peaks corresponding to the phosphorylated forms of the S262, S265, and S268 are indicated in black.

(C) Overlay of the ^{1}H projection of the ^{1}H, ^{15}N HSQC spectrum of free ^{15}N-labeled $FOXO4^{CR\text{-}PKB/AKT}$ WT or AKT-phosphorylated or AKT-CK1-phosphorylated at 100 μM (black, cyan, and orange lines, respectively) or bound to 1 equiv β-catenin (black, cyan, and orange dotted lines, respectively.

(D) HEK293T cells were transfected with FLAG-β-catenin- and biotin-labeled $FOXO4^{CR\text{-}PKB/AKT}$ (aa 252–281) or pSer262-$FOXO4^{CR\text{-}PKB/AKT}$ (aa 252–281, phosphorylated at 262) peptides were added to the cell lysate. Peptides were pulled down with magnetic streptavidin beads followed by immunoblotting with anti-FLAG or streptavidin- horseradish peroxidase (HRP).

(E and F) HEK293T cells were transfected with FLAG-β-catenin and HA-FOXO4 or HA-FOXO4 mutants, namely HA-FOXO4-S262A (E) or HA-FOXO4-S262D (F). Cells were treated with 100 μM H_2O_2 for 1 h, as indicated. Cell lysates were immunoprecipitated with anti-FLAG beads, followed by immunoblotting with anti-hemagglutinin (HA) and anti-FLAG antibodies.

(G) HEK293T cells were transfected with HA-FOXO4. Cells were treated with 50 μM H_2O_2 for different time periods, as indicated. Lysates were immunoblotted with anti-Ser 262p and anti-HA antibody, respectively.

(H) HEK293T cells were transfected with HA-FOXO4 or HA-FOXO4-S258A. Recombinant PP2A (Sigma-Aldrich, SRP5336) and PP2A boiled for 5 min (PP2A-dead) were added to the immunoprecipitates for 30 min at 37°C, followed by immunoblotting with anti-pS262 and anti-HA.

(I) HEK293T cells were transfected with FLAG-β-catenin and HA-FOXO4. Cells were treated with 100 μM H_2O_2 or 1 μM okadaic acid (Sigma, O9381) for 1 h, as indicated. Cell lysates were immunoprecipitated with 12CA5 (anti-HA) beads, followed by immunoblotting with anti-FLAG antibodies.

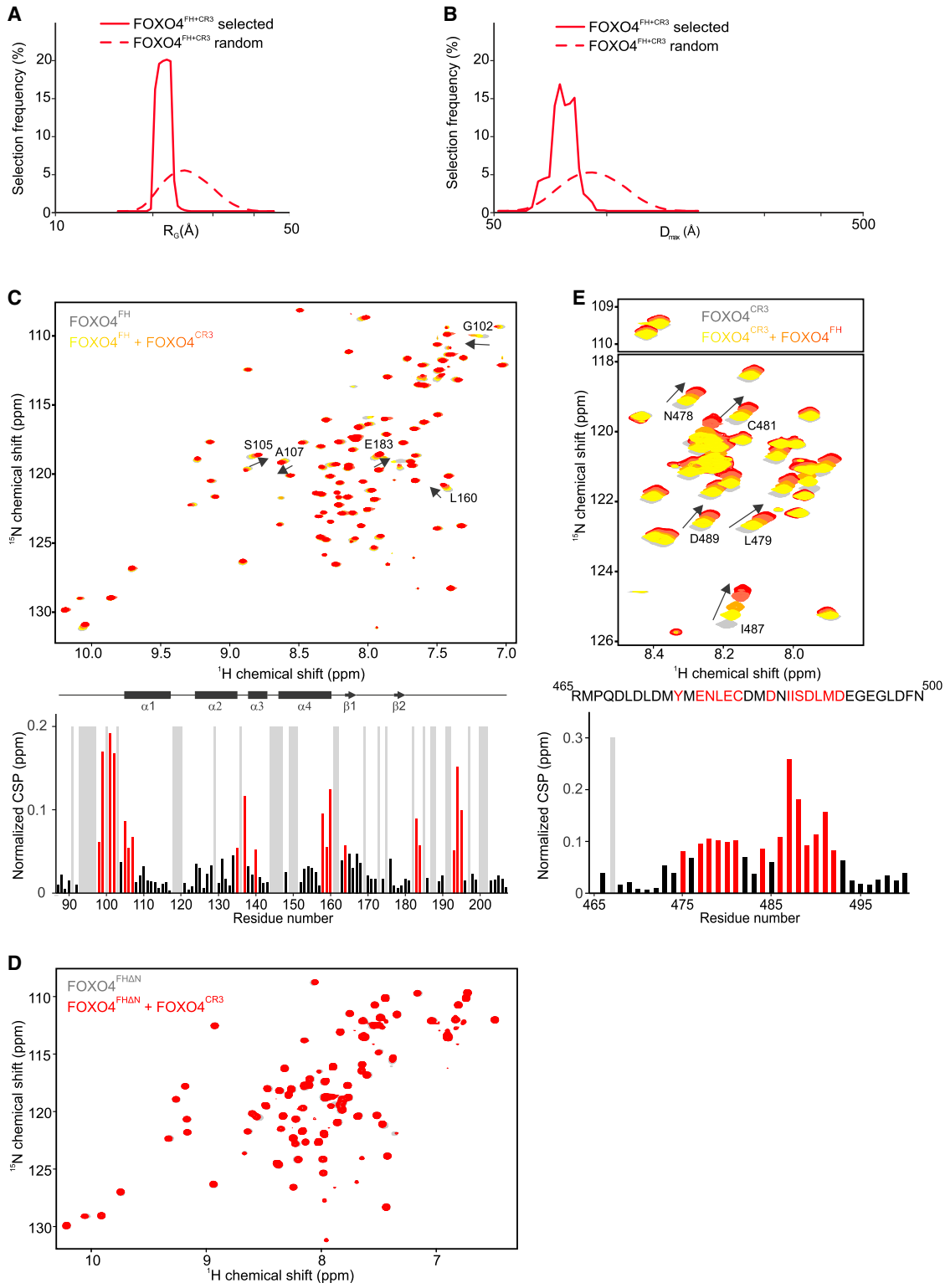

Figure 3. FOXO4 adopts an autoinhibited conformation, which weakens its DNA-binding efficiency

(A) EOM-based comparison of the radius of gyration (R_G) of the random pool of structures compared to the selected ensembles of $FOXO4^{FH+CR3}$.

(B) EOM-based comparison of the maximal distance (D_{max}) distributions of the random pool of structures compared to the selected ensembles of $FOXO4^{FH+CR3}$.

(C) ^{1}H, ^{15}N HSQC spectrum of ^{15}N-labeled $FOXO4^{FH}$ at 100 μM without (gray) or with 0.2, 0.4, 0.8, or 1 equiv $FOXO^{CR3}$ (yellow, orange, tomato, red, respectively).

(legend continued on next page)

and the CR3 (FOXO4^{FH+CR3}). Using small-angle X-ray scattering (SAXS) analysis, we characterized the conformational space sampled by FOXO4 using the ensemble optimization method (EOM) (Bernadó et al., 2007). Here, a pool of independent structures based on the aa sequence and available structural information is generated first. A genetic algorithm is then used to select an ensemble of structures that best describe the experimental SAXS data (for more details, see the Method details section). We identified the best ensembles concerning the agreement of experimental and back-calculated data. Figures 3A and 3B show, respectively, the comparison of the radius of gyration (R_G) and maximal distance (D_{max}) distributions of the random pool of structures compared to the selected ensembles. The EOM-reconstructed SAXS curve of the selected ensembles fits the raw scattering curve with an associated χ^2 of 3.2 (Figures S2A and S2B). Clearly, the selected ensemble shows a higher degree of compaction compared to the random pool, which indicates that there must be intramolecular interactions within FOXO4 that lead to compaction and hypothetically involving CR3 binding to the FH domain, as seen for FOXO3a.

To examine the molecular details of FOXO4 CR3 binding to FOXO4 FH, we used NMR spectroscopy. The stepwise addition of FOXO4^{CR3} to a solution of ^{15}N-labeled FOXO4^{FH} induced progressive CSPs of the FOXO4 FH ^{1}H, ^{15}N HSQC cross-peaks. The as affected upon CR3 addition cluster in (1) a region ranging from the N terminus to the beginning of helix α1 (W101–A107), (2) the C-terminal end of helix α3 (around L160), and (3) the C terminus (E183–G185) (Figure 3C). Similarly, comparison of the ^{1}H, ^{15}N HSQC spectra of FOXO4^{FH} alone or linked to the CR3 (FOXO4^{FH+CR3}) showed CSPs for the same set of FOXO4 aa (Figure S2C). As a control, deletion of the disordered N-terminal part of the FH domain from aa 86 to 104 (FOXO4$^{FH\Delta N}$) strongly impairs the binding of the CR3 showing that this part is essential for the back folding (Figure 3D). Conversely, stepwise addition of FOXO4^{FH} to a solution of ^{15}N-labeled FOXO4^{CR3} induced progressive CSPs of the FOXO4^{CR3} ^{1}H, ^{15}N HSQC cross-peaks. The residues affected upon the FOXO4^{FH} addition cluster in two distinct regions within the CR3 ranging from E477 to D482 and from I486 to L490, respectively (Figure 3E).

As attempts to crystallize the complex failed, we then generated a structural model of FOXO4^{FH} in complex with FOXO4^{CR3} using NMR-based structural restraints and the available structure of the FOXO4^{FH} as inputs. Due to intermediate exchange causing extensive line broadening of residues located within the binding interface, only a few nuclear Overhauser effect (NOE)-based distance restraints could be obtained. Nevertheless, additional distance restraints were obtained for 7 covalent paramagnetic labels attached at different positions within FOXO4^{FH} and FOXO4^{CR3}. Figure 4A shows an overlay of the resulting structures. FOXO4^{CR3} covers an extensive surface on FOXO4^{FH} via a network of hydrophobic and charge-based interactions (Figure 4B). In line with the CSP data (Figure 3C) and supported by the paramagnetic relaxation enhancement data, FOXO4^{CR3} recognition involves the disordered N/C termini, beginning of FOXO4^{FH} α-helix 1, and parts of α-helix 2 and α-helix 4. Comparison of our structural models with the 3D structure of the FOXO4 FH domain bound to DNA (PDB: 3L2C; Boura et al., 2010) shows that the binding surfaces of the FOXO4^{CR3} and DNA on the FH domain overlap, suggesting mutually exclusive interactions (Figure 4C). Therefore, we examined the effect of the observed FOXO4 intramolecular interaction on DNA binding. Isothermal titration calorimetry (ITC) analysis showed the binding of FOXO4^{FH} to a carboxy-terminal domain RNA polymerase II polypeptide A small phosphatase 2 (CTDSP2) response element 1 DNA (Kloet et al., 2015) with an associated K_D of 220 ± 17 nM (Table 1; Figure S3A). Deletion of the disordered region preceding the FH domain (FOXO4$^{FH\Delta N}$) and involved in CR3 recognition, resulted in a markedly decreased CTDSP2 binding affinity with an associated K_D of 4,371 ± 2,602 nM (Table 1; Figure S3B). Importantly, presence of the CR3 (FOXO4^{FH+CR3}) resulted in a 10-fold lower affinity of FOXO4 toward the CTDSP2 DNA (K_D of 3,320 ± 1,231 nM), thus confirming that intramolecular interaction between CR3 and the FH domain interferes with FOXO4 DNA binding (Table 1; Figure S3C). It is worth noting that the binding affinity of the CR3 region in *trans* to the FOXO4 FH domain is associated with a K_D of 1,172 ± 213 nM (Table 1; Figure S3D). Based on a polymer physics model and the size of the linker between the FH and CR3 region, we can estimate an effective concentration of 0.5 mM (van Dongen et al., 2007). This translates into an ∼,1000 times enhancement of the autoinhibition *in cis* and is on the order of the binding affinity of CTDSP2 to the FH domain (Table 1; Figure S3E). We therefore postulate that FOXO4 autoinhibition will efficiently compete with target DNAs.

Given that FOXO4 CR3 is involved in mediating both intramolecular contacts with the FH domain and intermolecular contacts with β-catenin, we hypothesized that the binding of β-catenin to FOXO4 can compete with the binding of the CR3 to the FH domain, thus releasing autoinhibition and enhancing DNA binding. To this end, we compared the DNA-binding affinities of the autoinhibited FOXO4^{FH+CR3} in the absence or presence of β-catenin. In line with our model, binding of FOXO4^{FH+CR3} to the CTDSP2 DNA is markedly enhanced in the presence of β-catenin, thus confirming that β-catenin binding to the CR3 can alleviate autoinhibition (Table 1; Figure S3F).

AKT and cellular redox induce multiple FOXO4 conformational changes *in vivo*

Our results suggest that in cells FOXO4 can exist in multiple different conformational states. To test whether FOXO4 is present in different conformations in cells, we generated a fluorescence resonance energy transfer (FRET) construct in which cyan fluorescent protein (CFP) is fused N-terminally and yellow fluorescent protein (YFP) is fused C-terminally to FOXO4 (Figure 5A), thereby creating CFP-FOXO4-YFP. The CFP-FOXO4-YFP construct is functional, as it interacts with β-catenin in a

(D) ^{1}H, ^{15}N HSQC spectrum of ^{15}N-labeled FOXO4$^{FH\Delta N}$ at 100 μM without (gray) or with equivalent of unlabeled FOXO4^{CR3} (red).
(E) ^{1}H, ^{15}N HSQC spectrum of ^{15}N-labeled FOXO4^{CR3} at 100 μM without (gray) or with 0.2, 0.4, 0.8, or 1 equiv unlabeled FOXO^{FH} (yellow, orange, tomato, red, respectively).
See also Table 1 and Figures S2 and S3.

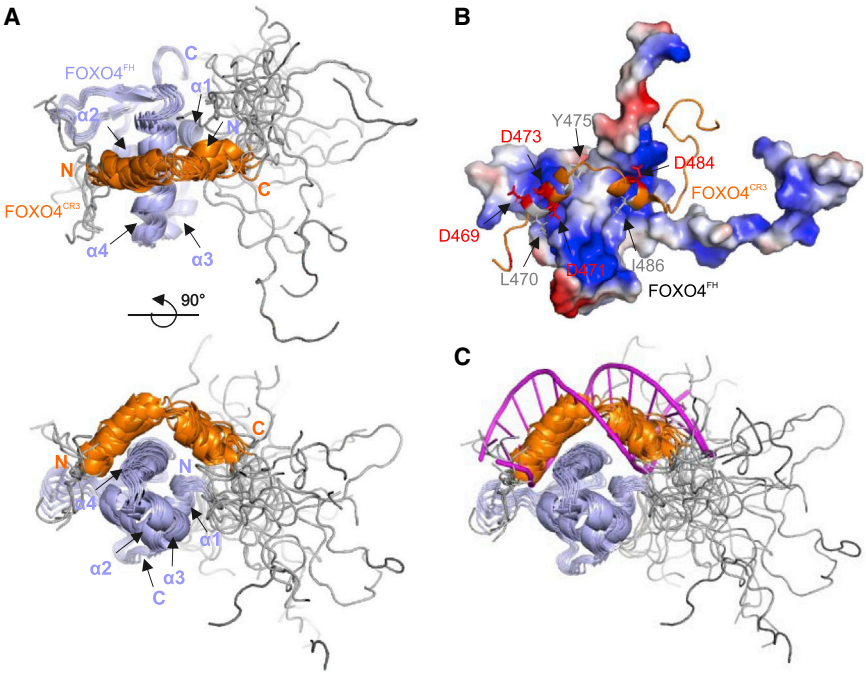

Figure 4. Structural model of FOXO4 autoinhibition

(A and B) Overlay of the 10 lowest energy structures of $FOXO4^{FH}$ in complex with $FOXO4^{CR3}$ using NMR-based structural restraints (A). The root mean square deviation (RMSD) of backbone heavy atom positions within rigid regions is 1.7 Å. Secondary structure elements and termini are indicated. The FH domain and CR3 region are blue and orange, respectively. Flexible regions of $FOXO4^{FH}$ and $FOXO4^{CR3}$ are gray. The complementary surface charge distribution of $FOXO4^{FH}$ and key CR3 residues involved in the interaction are shown in (B).

(C) Overlay of the 10 lowest energy structures of $FOXO4^{FH}$ in complex with $FOXO4^{CR3}$ overlaid with the crystallography-based structure of the FH domain of FOXO4 bound to DNA (PDB: 3L2C, right panel). The FH domain, CR3 region, and DNA are blue, orange, and magenta, respectively. Flexible regions of $FOXO4^{FH}$ and $FOXO4^{CR3}$ are gray.

See also Figure S4.

redox-dependent manner (Figure S5A), displays FOXO4-dependent transcription (Figure S5B) and is phosphorylated at the consensus AKT sites (Thr32 and Ser193) (Figure S5C). FOXOs shuttle between nucleus and cytosol, and upon ectopic expression, CFP-FOXO4-YFP is predominantly located in the nucleus. We determined the extent of nuclear FRET in untreated cells by measuring the increase in donor fluorescence (CFP) upon acceptor (YFP) photobleaching (Figure 5B; Wouters et al., 1998). The observed CFP-FOXO4-YFP FRET is due to an intramolecular interaction and not an intermolecular interaction, for example, due to dimerization/oligomerization, as we did not observe basal FRET or a change in FRET after PKB/AKT inhibition when we co-expressed YFP-FOXO4-YFP with CFP-FOXO4-CFP (Figure S5D).

To determine whether the activation of FOXO4 co-occurs with a change in FOXO4 conformation, we activated FOXO4 by the treatment of cells with either H_2O_2 to induce binding of co-factors such as β-catenin or by the inhibition of AKT activity. To exclude cell-type-specific effects, we tested FRET in two cell lines (HEK293T and U2OS) and we observed a significant increase in FRET efficiency upon FOXO4 activation (Figure 5C). To test whether autoinhibition through intramolecular interactions affects FRET efficiency, we deleted the region involved in CR3 recognition (Δ 91–104). Deletion of this region enhanced basal and H_2O_2-induced binding to β-catenin, likely due to increased accessibility to β-catenin once autoinhibition is impaired (Figure 5D). Interestingly, this correlated with a significant increase in basal FRET (Figure 5E). Of note, β-catenin is one of several co-factors for which binding to FOXO4 is increased after H_2O_2 treatment of cells (reviewed in Eijkelenboom and Burgering, 2013; van der Vos and Coffer, 2008). To address more specifically a role for β-catenin in the conformational change upon H_2O_2 treatment, we co-treated cells with a WNT pathway inhibitor (WNT-C59; Proffitt et al., 2013), thereby releasing β-catenin for binding to FOXO4. WNT pathway inhibition enhanced H_2O_2-induced FRET for CFP-FOXO4-YFP (Figure 5F), strongly suggesting the involvement of β-catenin binding in the conformational change induced by H_2O_2.

AKT-mediated phosphorylation regulates the binding of 14-3-3 proteins (Essers et al., 2005; Powell et al., 2002). Deletion of the autoinhibitory region (Δ 91–104) only partially impaired the response toward H_2O_2 or AKT inhibition. Deletion of the autoinhibitory region did not impair 14-3-3 binding, while AKT inhibition reduced 14-3-3 binding (Figure S5E). In addition, H_2O_2 treatment also resulted in loss of 14-3-3 binding (Figure S5E). In agreement with previous observations (Essers et al., 2004; Sunayama et al., 2005), this indicates that after H_2O_2 treatment the conformational changes observed are due to the combined loss of 14-3-3 binding and induced binding of co-factors such as β-catenin.

Next, we tested how binding between FOXO4 and 14-3-3 affects FOXO4 conformation; 14-3-3 binding is mediated by the first two AKT sites in FOXO4 (Thr32, Ser193) (Obsil et al., 2003). Thus, we generated a Thr32 to alanine mutant version and a Thr32 and Ser193 to double alanine mutant version of CFP-FOXO4-YFP. Both mutants show constitutive nuclear localization, as reported earlier (Kops et al., 1999). Importantly, these mutants showed progressive and significant increased basal nuclear FRET, in agreement with AKT inhibition increasing nuclear FRET of CFP-FOXO4-YFP (Figure 5G). Furthermore, this resulted in a lack of responsiveness toward AKT inhibition (Figure 5G). These results appear counterintuitive with respect to the model that 14-3-3 binding localizes FOXOs to the cytosol. However, earlier reports (Brownawell et al., 2001; Brunet et al., 2002) showed that AKT-mediated phosphorylation of FOXOs occurs in the nucleus and that 14-3-3 transits to the nucleus to bind phosphorylated FOXOs. Further supporting the nuclear role for

Table 1. Thermodynamic parameters of ITC titrations

Cell	Syringe	n	K_D (nM)	ΔH (kcal mol^{-1})	−TΔS (kcal mol^{-1})
$FOXO4^{FH}$ (Tris buffer)	CTDSP2	1.2 ± 0.1	220 ± 17	7.40 ± 0.05	−16.0 ± 0.1
$FOXO4^{FH+CR3}$ (Tris buffer)	CTDSP2	0.9 ± 0.1	3,320 ± 1231	6.32 ± 0.87	−13.4 ± 0.7
$FOXO4^{FH+CR3}$/β-catenin (Tris buffer)	CTDSP2	1.1 ± 0.1	345 ± 6	5.63 ± 0.14	−14.0 ± 0.1
$FOXO4^{FHΔN}$ (Tris buffer)	CTDSP2	1.1 ± 0.2	4,371 ± 2,602	4.01 ± 0.96	−11.0 ± 0.6
$FOXO4^{FH}$ (HEPES buffer)	CTDSP2	0.9 ± 0.1	4 ± 2	−3.12 ± 0.17	−7.0 ± 1.7
$FOXO4^{CR3}$ (Tris buffer)	$FOXO4^{FH}$	1.0 ± 0.1	1,172 ± 213	2.70 ± 0.12	−10.8 ± 0.2

The reported errors correspond to the SD of the triplicates.

AKT in regulating FOXOs is the suggestion that phosphorylation of the second AKT site (Ser193 in FOXO4) reduces DNA binding of FOXOs (Silhan et al., 2009). Thus, our FRET results are in agreement with these previous observations and show that nuclear FOXO4 also exists in a 14-3-3 bound conformation, which can undergo conformational change after AKT inhibition (increased FRET).

To validate our model further, we tested the effect of AKT activation, and in contrast to AKT inhibition, we observed a reduction in FRET, albeit minor (Figure S5F). This may indicate that under our experimental conditions, 14-3-3 binding to CFP-FOXO4-YFP is saturated, and that insulin/epidermal growth factor (EGF) signaling affects FOXO4 mostly in a 14-3-3-independent manner, in agreement with previous results (Cahill et al., 2001). AKT phosphorylation will ultimately result in FOXO4 shuttling to the cytosol, and the reduction of FRET after insulin/EGF treatment is further corroborated by our observation that in the cytosol steady state, FRET is lower compared to steady-state nuclear FRET (Figure S5G).

ICAT acts as molecular switch between WNT/TCF/LEF and FOXO signaling

FOXO4 binds a variety of regulatory proteins (Eijkelenboom and Burgering, 2013; van der Vos and Coffer, 2008) and this likely does not occur simultaneously. To study what interactors could specifically bind β-catenin when bound to FOXO4, we performed stable isotope labeling in culture (SILAC) and analyzed by mass spectrometry (MS) what proteins bind β-catenin in the presence versus absence of FOXO4. Interestingly, we observed strong binding of inhibitor of β-catenin and Tcf (ICAT)/β-catenin interacting protein 1 (CTNNBIP1) to β-catenin in the presence of FOXO4 (Figure 6A). The 3D structure of β-catenin/LEF-1 and β-catenin/ICAT indicates a partial overlap between the TCF/LEF-1 binding site and the ICAT binding site on β-catenin. Moreover, ICAT binding to β-catenin has been shown to inhibit the interaction with TCF (Graham et al., 2002). NMR showed that the C-terminal disordered region of FOXO4 does not compete with ICAT for binding to β-catenin *in vitro* (Figure 6B). Analytical ultracentrifugation analysis showed a small reduction of the free $FOXO^{C}$ ~1S species upon β-catenin addition as well as the appearance of an ~4.2-S peak, indicating β-catenin binding to $FOXO^{C}$. ICAT addition to $FOXO^{C}$/β-catenin resulted in an increase in the ~4.2 S peak intensity, suggesting that ICAT is binding to the $FOXO4^{C}$-β-catenin complex (Figure 6C). Furthermore, we found that in cells, ICAT overexpression inhibits the interaction between TCF and β-catenin, but, importantly, does not affect binding between FOXO4 and β-catenin and even enhances basal interaction (Figure 6D). The latter may also relate to the observation that ICAT has been shown to stabilize β-catenin expression by interfering with the formation of the APC/Axin-1 destruction complex (Ji et al., 2018). Thus, ICAT may serve to switch β-catenin signaling from TCF/LEF to FOXO4. When overexpressed, ICAT enhanced FOXO4 transcriptional activity, whereas ICAT and FOXO4 both efficiently repressed TCF transcriptional activity (Figure 6E).

DISCUSSION

TFs often contain IDRs, which can play unique roles in transcription. In this study, we examined the role of the FOXO4 IDR in mediating regulatory multivalent interactions with the folded co-factor β-catenin *in vitro* and *in vivo*. Initially, β-catenin was identified as a binding partner for FOXOs using the full C-terminal IDR of FOXO3 (Essers et al., 2005). Hence, the precise identification of the binding sites of β-catenin on FOXOs was unknown. Here, we show that FOXO4 binding to β-catenin involves multivalent interactions with three distinct FOXO4 regions; the structured DNA binding domain (FH) and the intrinsically disordered $CR^{PKB/AKT}$ and CR3 (Figure 1).

These three β-catenin binding sites are conserved among FOXOs, suggesting that these molecular determinants of binding also apply to other FOXO members (Figure S6). Besides FOXOs, other FOX proteins have been identified as β-catenin partners, including FOXM1, FOXP3, and the FH domain of FOXM1 (Yang et al., 2017; Zhang et al., 2011). This supports involvement of the FH domain in β-catenin recognition as a general feature for all FOX proteins.

Only a few interaction partners binding to the FOXO4 FH domain, besides DNA, are reported. Baar et al. (2017) identified p53 as binding to the FOXO4 FH domain, and this functions to maintain the viability of senescent cells. Interestingly, both binding of the FOXO4 CR3 identified in this study and binding of p53 affect similar residues within the FOXO4 FH, in particular its N-terminal region. This suggests that binding of the CR3 and p53 is mutually exclusive. Consequently, β-catenin could regulate the p53-FOXO4 interaction by competing with FOXO4 autoinhibition, which would in turn release the FOXO4 FH domain and enable p53 binding.

We show that β-catenin interaction with the C-terminal IDR of FOXO4 is mediated by the conserved $CR^{PKB/AKT}$ and CR3, which interact with β-catenin at different sites. FOXO transcriptional activity is regulated via recruitment of histone acetyl-transferases

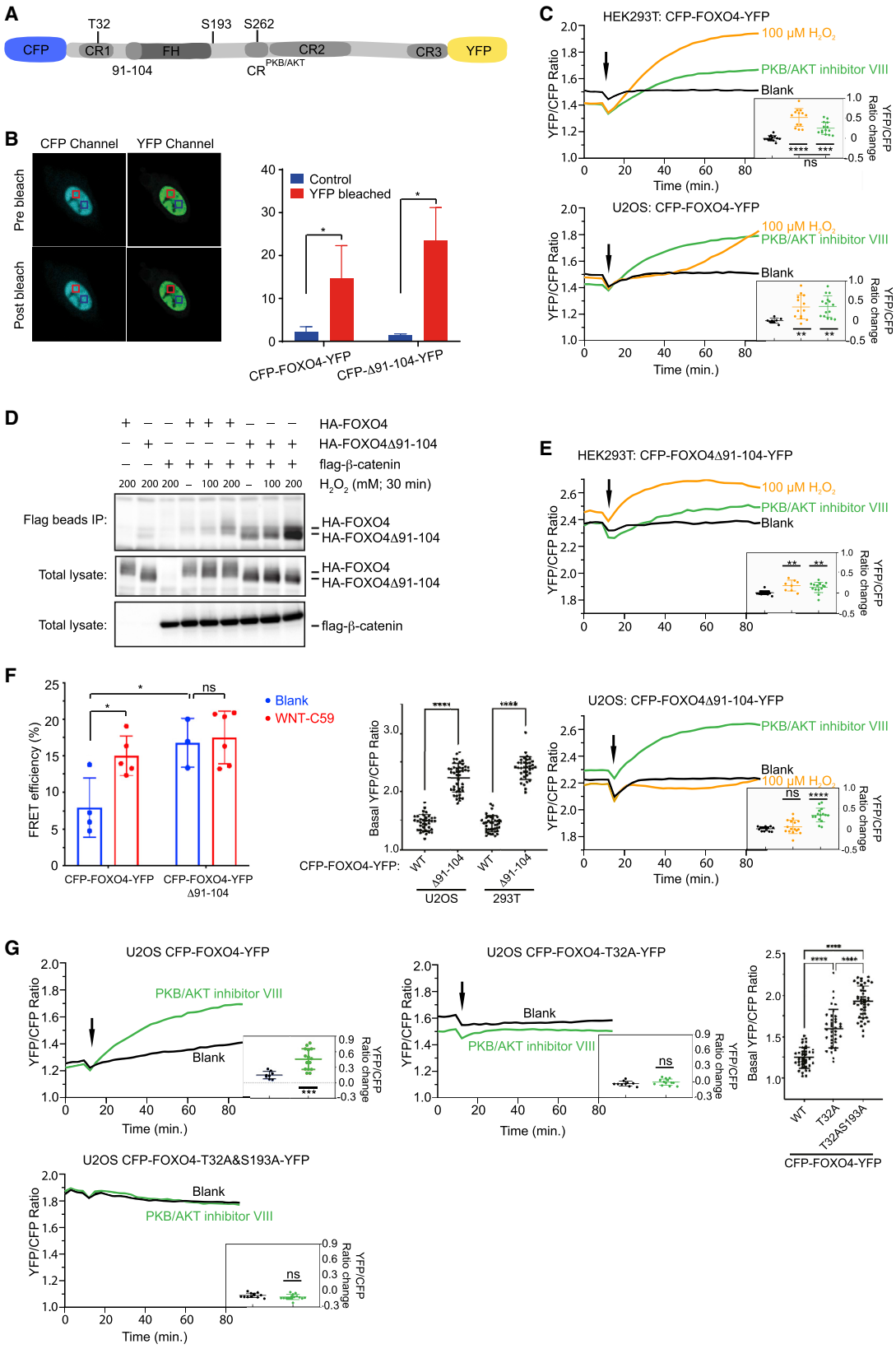

(legend on next page)

such as cyclic AMP (cAMP)-response element-binding protein (CBP/p300). This involves two conserved disordered regions within FOXO4 $CR^{PKB/AKT}$ and FOXO4 CR3 (Wang et al., 2012). Importantly, only the β-catenin binding site within CR3 overlaps with the CBP/p300 binding site. During transcription initiation, multiple co-regulators need to be recruited. Recently, β-catenin was shown to potentiate the recruitment of co-regulators, such as CBP/p300, to pluripotency loci and that this involves formation of phase-separated condensates (Hecht et al., 2000; Zamudio et al., 2019). Given that multivalent interactions involving IDRs are key for the formation of condensates, the FOXO4-β-catenin-CBP/p300 interaction network could be essential for the priming and stabilization of these condensates by enhancing the cooperative and multivalent interactions between co-regulators at sites of transcription.

Regulation of FOXOs by the PI3K/AKT pathway through AKT-mediated phosphorylation (Thr32, Ser197, and Ser262 for FOXO4) leads to the inhibition of FOXO transcriptional activity (Tzivion et al., 2011). Phosphorylation at Thr32 and Ser197 allows 14-3-3 binding and subsequent masking of the FOXO4 nuclear localization signal, leading to the redistribution of FOXOs to the cytosol (Obsil et al., 2003; Obsilova et al., 2005). AKT-mediated phosphorylation of the third site is a priming event allowing CK1 phosphorylation of two additional sites (Ser265 and Ser268 for FOXO4) and is also involved in the nuclear exclusion of FOXOs (Rena et al., 2002, 2004). Here, we show that AKT is sufficient for mediating the phosphorylation of FOXO4-$CR^{PKB/AKT}$ Ser262 and acts as a priming phosphorylation event allowing CK1-mediated phosphorylation of Ser265 and Ser268 *in vitro* using recombinant proteins. Moreover, we show that phosphorylation of these sites impairs FOXO4 binding to β-catenin both *in vitro* and *in vivo* (Figure 2), which is in line with the presence of an autoinhibited conformation in which the FOXO4 CR3 is inaccessible for β-catenin binding. Impairment of FOXO4 binding to β-catenin in the nucleus could therefore facilitate its nuclear exclusion and participate in AKT-mediated inhibition of FOXO4 transcriptional activity.

Wang et al. (2008) previously showed that the C-terminal transactivation domain of FOXO3 (CR3) directly interacts with the FH domain on a surface that overlaps with the DNA binding site, suggesting an autoinhibitory conformation of FOXO3. Here, we show that in line with FOXO3, FOXO4 CR3 binds to the FOXO4 FH domain involving a binding interface that overlaps with the known DNA binding site. In turn, DNA binding affinity is reduced (Table 1; Figures S3A and S3C), and this may be important in preventing unspecific binding of FOXOs to DNA. Furthermore, we show that binding of β-catenin to the CR3 is essential to expose the FH domain for efficient DNA binding and therefore provide a mechanistic explanation as to how β-catenin acts as a trans-activator of FOXO signaling. Given the conservation of both the CR3 and the FH domain in FOXO1, FOXO3, and FOXO6 (Figure S6), it is tempting to speculate that this mechanism of regulation of FOXO4 activity is conserved among FOXOs.

To study the consequences of the *in vitro*-defined interactions to the dynamics and structure of FOXOs *in vivo*, we designed a FRET FOXO4 construct, the rationale being that changes in FRET signal are a good proxy for changes in the conformation of FOXO4. We observed that activation of FOXO4 results in a conformational change. Surprisingly, we observed an increase in the FRET ratio upon activation. The intermolecular interaction between the CR3 domain and the FH domain in the inhibited state would bring CFP and YFP into close proximity, suggesting high FRET efficiency, possibly higher relative to the activated state. As we observe this not to be the case, we conclude that apparently, FRET is determined not only by proximity but also by alignment of the FRET pair. The N-terminal domain of FOXO4 is considerably shorter in length than the C-terminal domain and this apparently positions the FRET pair in the autoinhibited state in close proximity but not aligned properly, resulting in lower FRET efficiency.

Moreover, FOXO4 can be present in different conformations within the nucleus. DNA binding of FOXO4 is precluded by either binding to 14-3-3 or by adopting the autoinhibitory conformation. Our results do not allow us to conclude whether these are two independent conformations. However, H_2O_2 treatment results in the loss of 14-3-3 binding, similar to AKT inhibition, and induces the binding of β-catenin, which is not observed after AKT

Figure 5. FOXO4 adopts multiple conformations *in vivo*

(A) Schematic representation of the CFP-FOXO4-YFP FRET probe. Position of the fluorophores (CFP and YFP), the autoinhibitory region (aa 91–104), the AKT phosphorylation sites (T32, S193, and S262), and the CR-PKB/AKT and CR3 regions involved in β-catenin binding are indicated.

(B) U2OS cells were transfected with CFP-FOXO4-YFP or CFP-FOXO4-Δ91–104-YFP. For a typical measurement, the nuclear areas (control and photobleached) before and after photobleaching are indicated. The increase in CFP intensity after YFP photobleaching was used to determine FRET efficiency. Data represent means ± SDs, n = 3.

(C) HEK293T cells were transfected with CFP-FOXO4-YFP and when stable, YFP and CFP emission was observed. H_2O_2 or AKT inhibitor VIII was added (indicated by the arrow), and YFP and CFP emission was followed over time and the ratio calculated. Each panel shows a typical trace for each experimental condition, and the inset shows the change in FRET ratio (plateau level–starting level) for multiple traces, whereby each dot represents the result of 1 trace. Traces were obtained from different experiments (n = 3). Blot graphs represent means ± SDs. At least 8 cells were analyzed per condition.

(D) HEK293T cells were transfected with FLAG-β-catenin and HA-FOXO4 or HA-FOXO4Δ91–104. Cells were treated with H_2O_2 (100 μM) for 30 min as indicated. Binding between β-catenin and FOXO4 was determined by immunoprecipitation of FLAG-β-catenin with anti-FLAG beads, followed by immunoblotting with anti-HA antibodies.

(E) HEK293T and U2OS cells were transfected with CFP-FOXO4-Δ91–104-YFP. Cells were treated with 100 μM H_2O_2 or AKT inhibitor VIII and analyzed as described in (C). The inset represents results of multiple experiments (n = 3).

(F) U2OS cells were transfected with CFP-FOXO4-YFP or CFP-FOXO4-Δ91–104-YFP. FRET efficiency was determined as in Figure 4B. Treatment with WNT-C59 (final concentration, 5 μM) was for 16 h before performing the photobleaching (n = 3). Data represent the means ± SDs.

(G) U2OS cells were transfected with CFP-FOXO4-YFP, or the AKT site mutants CFP-FOXO4-T32A-YFP, or the double mutant CFP-FOXO4-T32&S193A-YFP. FRET analysis was as in (C) and (E). At least 8 cells were analyzed.

See also Figure S5.

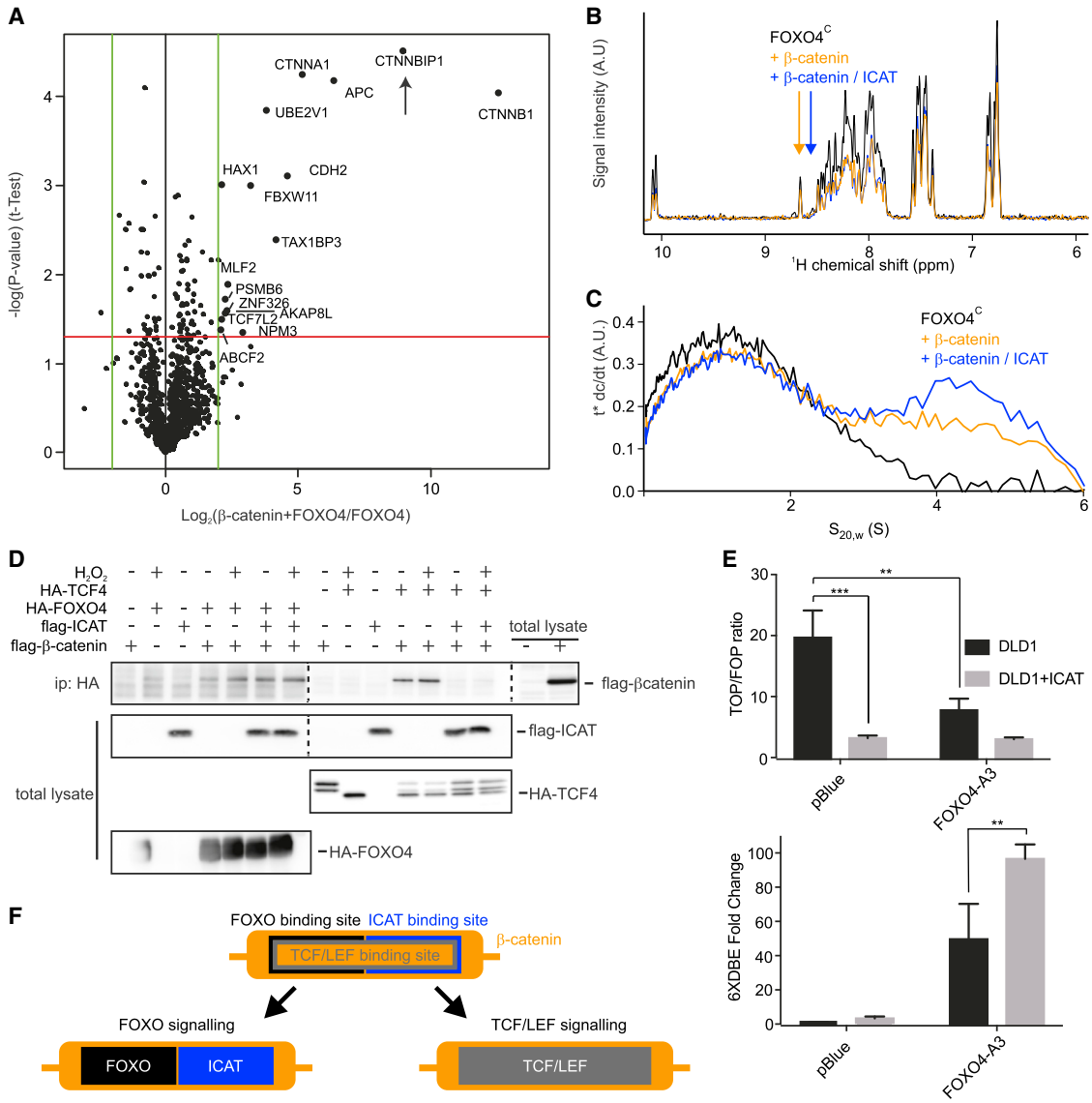

Figure 6. ICAT, molecular switch between Tcf/Lef and FOXO signaling

(A) HEK293T cells stably labeled with heavy/light arginine and lysine were transfected with GFP-FOXO4 alone or co-transfected with GFP-FOXO4 and FLAG-β-catenin. After GFP pull-down, co-precipitated proteins were identified by liquid chromatography (LC)-tandem MS (MS/MS) and data were processed as described in Method details. Upper right quadrant represents potential interacting proteins with FOXO4 in the presence of β-catenin.

(B) Overlay of the ^{1}H projection of the ^{1}H, ^{15}N HSQC spectrum of free ^{15}N-labeled $FOXO4^{C}$ at 50 μM or in the presence of 1 equiv β-catenin or 1:1 equiv ICAT:β-catenin (black, orange, and blue lines, respectively).

(C) Ultracentrifugation analysis of free fluorescein isothiocyanate (FITC)-labeled $FOXO^{C}$ at 0.2 μM or in the presence of 45 μM of β-catenin or in the presence of 45 and 90 μM of β-catenin and ICAT, respectively (black, orange, and blue lines, respectively).

(D) HEK293T cells were transfected with FLAG-β-catenin, FLAG-ICAT, HA-FOXO4, or HA-TCF4, as indicated. Cell lysates were immunoprecipitated with anti-HA beads, following immunoblotting with anti-FLAG. Total lysates indicate expression of HA-FOXO4, HA-TCF4, or FLAG-ICAT.

(E) DLD1 cells were transfected with TOP/FOP reporters for measurement of TCF transcriptional activity or 6xDBE for FOXO transcriptional activity. Indicated constructs were co-transfected and luciferase activity was measured as described. Data represent means ± SDs.

(F) Model showing differential binding regions of ICAT, TCF, and FOXO4 on β-catenin.

inhibition. Our *in vitro* data strongly suggest that one function of β-catenin binding is to prevent folding into the autoinhibited state, and we interpret these data to suggest that the autoinhibitory state functions as a backup inhibition mechanism when FOXO4 is not bound to 14-3-3. Full DNA binding is then only acquired when FOXO4 binds additional co-factors such as β-catenin. This interpretation is also supported by the observations using the Δ91–104 FOXO4 mutant. This mutant displays a change in FRET compared to the wild-type protein and remains responsive to AKT inhibition, which induces a further change in FRET.

Our FRET data also suggest that 14-3-3 binding and regulation of FOXO4 by H_2O_2 and AKT signaling occurs in the nucleus and that a considerable fraction of FOXO4 is bound to 14-3-3 within the nucleus. The FRET signal of FOXO4 localized in the cytosol bound to 14-3-3 also differs from FOXO4 bound to 14-3-3 in the nucleus, suggesting that additional co-factor binding is regulated by PI3K signaling when localizing FOXO4 to the cytosol. Whether this cytosolic conformation difference relates to the suggested non-nuclear functions of FOXOs (Medema and Jäättelä, 2010; Zhao et al., 2010) remains to be determined.

Here, we show that ICAT binding to β-catenin does not interfere with FOXO4 binding, providing a mechanistic explanation as to how β-catenin may switch from TCF/LEF to FOXO binding (Figure 6F). This ICAT-mediated molecular switch may direct cell fate from TCF/LEF-mediated cellular proliferation toward FOXO-mediated cell-cycle arrest. Aberrant WNT signaling has been reported for many cancers (Cheng et al., 2019). Targeting ICAT to favor switching of β-catenin from TCF/LEF to FOXO may be an attractive, indirect way of manipulating WNT signaling in cancer, as this would also actively engage cell-cycle inhibitory FOXO-dependent pathways.

Summarizing, we show that the FOXO4 IDR mediates multivalent interactions and that is important for its function. We hypothesize that similar β-catenin-dependent mechanisms apply to other TFs. In the future, it will be important to study whether the molecular interface regulating the interaction between β-catenin, TFs, and transcriptional co-regulators can be used to develop specialized anticancer drugs.

STAR★METHODS

Detailed methods are provided in the online version of this paper and include the following:

- KEY RESOURCES TABLE
- RESOURCE AVAILABILITY
  - Lead contact
  - Materials availability
  - Data and code availability
- EXPERIMENTAL MODEL AND SUBJECT DETAILS
- METHOD DETAILS
  - Constructs and transfections
  - Protein expression and purification
  - Paramagnetic labeling
  - Oligos
  - Peptides
  - Isothermal titration calorimetry (ITC)
  - Estimation of the effective molarity
  - NMR spectroscopy
  - Structure determination
  - Phosphorylation assays in HEK293T cell extracts
  - *In vitro*, AKT and CK1 phosphorylation assays
  - SAXS
  - Ultracentrifugation analysis
  - Immunoprecipitation
  - FRET
  - FRET validation by photobleaching
  - Dual luciferase assay
  - SILAC labeling
  - Mass spectrometry
  - LC-MS/MS and data analysis
- QUANTIFICATION AND STATISTICAL ANALYSIS

SUPPLEMENTAL INFORMATION

Supplemental information can be found online at https://doi.org/10.1016/j.celrep.2021.109446.

ACKNOWLEDGMENTS

Work in the Burgering Laboratory is financially supported by Oncode. T.G. was supported by the China Scholarship Council from 2016 to 2020 (no. 201604910624). We wish to thank Dr. Tobias Dansen and Jurian Schuijer for discussion, Prof. Madelon Maurice for providing WNT-C59, Dr. HarmJan Vos for performing MS, Dr. Bas Ponsioen for help and advice on the FRET analysis, and Ing. Lydia Smits for technical support. T.M. was supported by Austrian Science Foundation grants P28854, I3792, and DK-MCD W1226; Austrian Research Promotion Agency (FFG) grants 864690 and 870454; the Integrative Metabolism Research Center Graz; Austrian Infrastructure Program 2016/2017, the Styrian government (Zukunftsfonds), and BioTechMed-Graz (Flagship project).

AUTHOR CONTRIBUTIONS

B.B., G.R., and E.S. performed the protein expression and purification. B.B. and E.S. performed the NMR experiments. B.B. performed the ITC experiments and the fluorescence anisotropy experiments. H.G.H. performed the SAXS experiments. M.V. performed the analytical ultracentrifugation (AUC) experiments. T.G. and D.H. performed the co-immunoprecipitation experiments. T.G. performed the luciferase assay, the FRET experiments, and the MS experiments. B.B., T.G., H.G.H., T.M., G.R., E.S., K.R., and B.M.T.B. prepared the manuscript.

DECLARATION OF INTERESTS

The authors declare no competing interests.

Received: August 17, 2020
Revised: April 15, 2021
Accepted: July 2, 2021
Published: July 27, 2021

REFERENCES

Almeida, M., Han, L., Martin-Millan, M., O'Brien, C.A., and Manolagas, S.C. (2007). Oxidative stress antagonizes Wnt signaling in osteoblast precursors by diverting beta-catenin from T cell factor- to forkhead box O-mediated transcription. J. Biol. Chem. *282*, 27298–27305.

Baar, M.P., Brandt, R.M.C., Putavet, D.A., Klein, J.D.D., Derks, K.W.J., Bourgeois, B.R.M., Stryeck, S., Rijksen, Y., van Willigenburg, H., Feijtel, D.A., et al. (2017). Targeted Apoptosis of Senescent Cells Restores Tissue Homeostasis in Response to Chemotoxicity and Aging. Cell *169*, 132–147.e16.

Bah, A., and Forman-Kay, J.D. (2016). Modulation of Intrinsically Disordered Protein Function by Post-translational Modifications. J. Biol. Chem. *291*, 6696–6705.

Battiste, J.L., and Wagner, G. (2000). Utilization of site-directed spin labeling and high-resolution heteronuclear nuclear magnetic resonance for global fold determination of large proteins with limited nuclear overhauser effect data. Biochemistry *39*, 5355–5365.

Bernadó, P., Mylonas, E., Petoukhov, M.V., Blackledge, M., and Svergun, D.I. (2007). Structural characterization of flexible proteins using small-angle X-ray scattering. J. Am. Chem. Soc. *129*, 5656–5664.

Biggs, W.H., 3rd, Meisenhelder, J., Hunter, T., Cavenee, W.K., and Arden, K.C. (1999). Protein kinase B/Akt-mediated phosphorylation promotes nuclear exclusion of the winged helix transcription factor FKHR1. Proc. Natl. Acad. Sci. USA *96*, 7421–7426.

Boija, A., Klein, I.A., Sabari, B.R., Dall'Agnese, A., Coffey, E.L., Zamudio, A.V., Li, C.H., Shrinivas, K., Manteiga, J.C., Hannett, N.M., et al. (2018). Transcription Factors Activate Genes through the Phase-Separation Capacity of Their Activation Domains. Cell *175*, 1842–1855.e16.

Boura, E., Rezabkova, L., Brynda, J., Obsilova, V., and Obsil, T. (2010). Structure of the human FOXO4-DBD-DNA complex at 1.9 Å resolution reveals new details of FOXO binding to the DNA. Acta Crystallogr. D Biol. Crystallogr. *66*, 1351–1357.

Bourgeois, B., and Madl, T. (2018). Regulation of cellular senescence via the FOXO4-p53 axis. FEBS Lett. *592*, 2083–2097.

Brent, M.M., Anand, R., and Marmorstein, R. (2008). Structural basis for DNA recognition by FoxO1 and its regulation by posttranslational modification. Structure *16*, 1407–1416.

Brodsky, S., Jana, T., Mittelman, K., Chapal, M., Kumar, D.K., Carmi, M., and Barkai, N. (2020). Intrinsically Disordered Regions Direct Transcription Factor In Vivo Binding Specificity. Mol. Cell *79*, 459–471.e4.

Brownawell, A.M., Kops, G.J., Macara, I.G., and Burgering, B.M. (2001). Inhibition of nuclear import by protein kinase B (Akt) regulates the subcellular distribution and activity of the forkhead transcription factor AFX. Mol. Cell. Biol. *21*, 3534–3546.

Brunet, A., Bonni, A., Zigmond, M.J., Lin, M.Z., Juo, P., Hu, L.S., Anderson, M.J., Arden, K.C., Blenis, J., and Greenberg, M.E. (1999). Akt promotes cell survival by phosphorylating and inhibiting a Forkhead transcription factor. Cell *96*, 857–868.

Brunet, A., Kanai, F., Stehn, J., Xu, J., Sarbassova, D., Frangioni, J.V., Dalal, S.N., DeCaprio, J.A., Greenberg, M.E., and Yaffe, M.B. (2002). 14-3-3 transits to the nucleus and participates in dynamic nucleocytoplasmic transport. J. Cell Biol. *156*, 817–828.

Brünger, A.T., Adams, P.D., Clore, G.M., DeLano, W.L., Gros, P., Grosse-Kunstleve, R.W., Jiang, J.S., Kuszewski, J., Nilges, M., Pannu, N.S., et al. (1998). Crystallography & NMR system: a new software suite for macromolecular structure determination. Acta Crystallogr. D Biol. Crystallogr. *54*, 905–921.

Burgering, B.M., and Medema, R.H. (2003). Decisions on life and death: FOXO Forkhead transcription factors are in command when PKB/Akt is off duty. J. Leukoc. Biol. *73*, 689–701.

Cahill, C.M., Tzivion, G., Nasrin, N., Ogg, S., Dore, J., Ruvkun, G., and Alexander-Bridges, M. (2001). Phosphatidylinositol 3-kinase signaling inhibits DAF-16 DNA binding and function via 14-3-3-dependent and 14-3-3-independent pathways. J. Biol. Chem. *276*, 13402–13410.

Cheng, X., Xu, X., Chen, D., Zhao, F., and Wang, W. (2019). Therapeutic potential of targeting the Wnt/β-catenin signaling pathway in colorectal cancer. Biomed. Pharmacother. *110*, 473–481.

Clevers, H., and Nusse, R. (2012). Wnt/β-catenin signaling and disease. Cell *149*, 1192–1205.

Davy, P.M.C., Allsopp, R.C., Donlon, T.A., Morris, B.J., Willcox, D.C., and Willcox, B.J. (2018). FOXO3 and Exceptional Longevity: Insights From Hydra to Humans. Curr. Top. Dev. Biol. *127*, 193–212.

de Keizer, P.L., Packer, L.M., Szypowska, A.A., Riedl-Polderman, P.E., van den Broek, N.J., de Bruin, A., Dansen, T.B., Marais, R., Brenkman, A.B., and Burgering, B.M. (2010). Activation of forkhead box O transcription factors by oncogenic BRAF promotes p21cip1-dependent senescence. Cancer Res. *70*, 8526–8536.

de la Roche, M., Rutherford, T.J., Gupta, D., Veprintsev, D.B., Saxty, B., Freund, S.M., and Bienz, M. (2012). An intrinsically labile α-helix abutting the BCL9-binding site of β-catenin is required for its inhibition by carnosic acid. Nat. Commun. *3*, 680.

Dyson, H.J., and Wright, P.E. (2005). Intrinsically unstructured proteins and their functions. Nat. Rev. Mol. Cell Biol. *6*, 197–208.

Eijkelenboom, A., and Burgering, B.M. (2013). FOXOs: signalling integrators for homeostasis maintenance. Nat. Rev. Mol. Cell Biol. *14*, 83–97.

Essers, M.A.G., Weijzen, S., de Vries-Smits, A.M.M., Saarloos, I., de Ruiter, N.D., Bos, J.L., and Burgering, B.M.T. (2004). FOXO transcription factor activation by oxidative stress mediated by the small GTPase Ral and JNK. EMBO J. *23*, 4802–4812.

Essers, M.A., de Vries-Smits, L.M., Barker, N., Polderman, P.E., Burgering, B.M., and Korswagen, H.C. (2005). Functional interaction between beta-catenin and FOXO in oxidative stress signaling. Science *308*, 1181–1184.

Graham, T.A., Clements, W.K., Kimelman, D., and Xu, W. (2002). The crystal structure of the beta-catenin/ICAT complex reveals the inhibitory mechanism of ICAT. Mol. Cell *10*, 563–571.

Guo, X., Bulyk, M.L., and Hartemink, A.J. (2012). Intrinsic disorder within and flanking the DNA-binding domains of human transcription factors. Pac. Symp. Biocomput., 104–115.

Habchi, J., Tompa, P., Longhi, S., and Uversky, V.N. (2014). Introducing protein intrinsic disorder. Chem. Rev. *114*, 6561–6588.

Hannenhalli, S., and Kaestner, K.H. (2009). The evolution of Fox genes and their role in development and disease. Nat. Rev. Genet. *10*, 233–240.

Hartlmüller, C., Spreitzer, E., Göbl, C., Falsone, F., and Madl, T. (2019). NMR characterization of solvent accessibility and transient structure in intrinsically disordered proteins. J. Biomol. NMR *73*, 305–317.

Hayes, D.B., and Stafford, W.F. (2010). SEDVIEW, real-time sedimentation analysis. Macromol. Biosci. *10*, 731–735.

Hecht, A., Vleminckx, K., Stemmler, M.P., van Roy, F., and Kemler, R. (2000). The p300/CBP acetyltransferases function as transcriptional coactivators of beta-catenin in vertebrates. EMBO J. *19*, 1839–1850.

Hoogeboom, D., Essers, M.A., Polderman, P.E., Voets, E., Smits, L.M., and Burgering, B.M. (2008). Interaction of FOXO with beta-catenin inhibits beta-catenin/T cell factor activity. J. Biol. Chem. *283*, 9224–9230.

Inukai, S., Kock, K.H., and Bulyk, M.L. (2017). Transcription factor-DNA binding: beyond binding site motifs. Curr. Opin. Genet. Dev. *43*, 110–119.

Ji, L., Lu, B., Wang, Z., Yang, Z., Reece-Hoyes, J., Russ, C., Xu, W., and Cong, F. (2018). Identification of ICAT as an APC Inhibitor, Revealing Wnt-Dependent Inhibition of APC-Axin Interaction. Mol. Cell *72*, 37–47.e4.

Kloet, D.E., Polderman, P.E., Eijkelenboom, A., Smits, L.M., van Triest, M.H., van den Berg, M.C., Groot Koerkamp, M.J., van Leenen, D., Lijnzaad, P., Holstege, F.C., and Burgering, B.M. (2015). FOXO target gene CTDSP2 regulates cell cycle progression through Ras and p21(Cip1/Waf1). Biochem. J. *469*, 289–298.

Klotz, L.O., Sánchez-Ramos, C., Prieto-Arroyo, I., Urbánek, P., Steinbrenner, H., and Monsalve, M. (2015). Redox regulation of FoxO transcription factors. Redox Biol. *6*, 51–72.

Kops, G.J., de Ruiter, N.D., De Vries-Smits, A.M., Powell, D.R., Bos, J.L., and Burgering, B.M. (1999). Direct control of the Forkhead transcription factor AFX by protein kinase B. Nature *398*, 630–634.

Kops, G.J., Medema, R.H., Glassford, J., Essers, M.A., Dijkers, P.F., Coffer, P.J., Lam, E.W., and Burgering, B.M. (2002). Control of cell cycle exit and entry by protein kinase B-regulated forkhead transcription factors. Mol. Cell. Biol. *22*, 2025–2036.

Lam, E.W., Brosens, J.J., Gomes, A.R., and Koo, C.Y. (2013). Forkhead box proteins: tuning forks for transcriptional harmony. Nat. Rev. Cancer *13*, 482–495.

Lambert, S.A., Jolma, A., Campitelli, L.F., Das, P.K., Yin, Y., Albu, M., Chen, X., Taipale, J., Hughes, T.R., and Weirauch, M.T. (2018). The Human Transcription Factors. Cell *172*, 650–665.

Linge, J.P., Habeck, M., Rieping, W., and Nilges, M. (2003). ARIA: automated NOE assignment and NMR structure calculation. Bioinformatics *19*, 315–316.

Liu, H., Fergusson, M.M., Wu, J.J., Rovira, I.I., Liu, J., Gavrilova, O., Lu, T., Bao, J., Han, D., Sack, M.N., and Finkel, T. (2011). Wnt signaling regulates hepatic metabolism. Sci. Signal. *4*, ra6.

MacDonald, B.T., Tamai, K., and He, X. (2009). Wnt/beta-catenin signaling: components, mechanisms, and diseases. Dev. Cell *17*, 9–26.

Madeira, F., Park, Y.M., Lee, J., Buso, N., Gur, T., Madhusoodanan, N., Basutkar, P., Tivey, A.R.N., Potter, S.C., Finn, R.D., and Lopez, R. (2019). The EMBL-EBI search and sequence analysis tools APIs in 2019. Nucleic Acids Res. *47* (*W1*), W636–W641.

Manning, B.D., and Toker, A. (2017). AKT/PKB Signaling: Navigating the Network. Cell *169*, 381–405.

Medema, R.H., and Jäättelä, M. (2010). Cytosolic FoxO1: alive and killing. Nat. Cell Biol. *12*, 642–643.

Ng, S.S., Mahmoudi, T., Danenberg, E., Bejaoui, I., de Lau, W., Korswagen, H.C., Schutte, M., and Clevers, H. (2009). Phosphatidylinositol 3-kinase signaling does not activate the wnt cascade. J. Biol. Chem. *284*, 35308–35313.

Nilges, M. (1995). Calculation of protein structures with ambiguous distance restraints. Automated assignment of ambiguous NOE crosspeaks and disulphide connectivities. J. Mol. Biol. *245*, 645–660.

Obsil, T., Ghirlando, R., Anderson, D.E., Hickman, A.B., and Dyda, F. (2003). Two 14-3-3 binding motifs are required for stable association of Forkhead transcription factor FOXO4 with 14-3-3 proteins and inhibition of DNA binding. Biochemistry *42*, 15264–15272.

Obsilova, V., Vecer, J., Herman, P., Pabianova, A., Sulc, M., Teisinger, J., Boura, E., and Obsil, T. (2005). 14-3-3 Protein interacts with nuclear localization sequence of forkhead transcription factor FoxO4. Biochemistry *44*, 11608–11617.

Ponsioen, B., Post, J.B., Buissant des Amorie, J.R., Laskaris, D., van Ineveld, R.L., Kersten, S., Bertotti, A., Sassi, F., Sipieter, F., Cappe, B., et al. (2021). Quantifying single-cell ERK dynamics in colorectal cancer organoids reveals EGFR as an amplifier of oncogenic MAPK pathway signalling. Nat Cell Biol *23*, 377–390.

Powell, D.W., Rane, M.J., Chen, Q., Singh, S., and McLeish, K.R. (2002). Identification of 14-3-3zeta as a protein kinase B/Akt substrate. J. Biol. Chem. *277*, 21639–21642.

Proffitt, K.D., Madan, B., Ke, Z., Pendharkar, V., Ding, L., Lee, M.A., Hannoush, R.N., and Virshup, D.M. (2013). Pharmacological inhibition of the Wnt acyltransferase PORCN prevents growth of WNT-driven mammary cancer. Cancer Res. *73*, 502–507.

Rao, P., Pang, M., Qiao, X., Yu, H., Wang, H., Yang, Y., Ren, X., Hu, M., Chen, T., Cao, Q., et al. (2019). Promotion of β-catenin/Foxo1 signaling ameliorates renal interstitial fibrosis. Lab. Invest. *99*, 1689–1701.

Rena, G., Guo, S., Cichy, S.C., Unterman, T.G., and Cohen, P. (1999). Phosphorylation of the transcription factor forkhead family member FKHR by protein kinase B. J. Biol. Chem. *274*, 17179–17183.

Rena, G., Woods, Y.L., Prescott, A.R., Peggie, M., Unterman, T.G., Williams, M.R., and Cohen, P. (2002). Two novel phosphorylation sites on FKHR that are critical for its nuclear exclusion. EMBO J. *21*, 2263–2271.

Rena, G., Bain, J., Elliott, M., and Cohen, P. (2004). D4476, a cell-permeant inhibitor of CK1, suppresses the site-specific phosphorylation and nuclear exclusion of FOXO1a. EMBO Rep. *5*, 60–65.

Sabari, B.R., Dall'Agnese, A., Boija, A., Klein, I.A., Coffey, E.L., Shrinivas, K., Abraham, B.J., Hannett, N.M., Zamudio, A.V., Manteiga, J.C., et al. (2018). Coactivator condensation at super-enhancers links phase separation and gene control. Science *361*, eaar3958.

Schindelin, J., Arganda-Carreras, I., Frise, E., Kaynig, V., Longair, M., Pietzsch, T., Preibisch, S., Rueden, C., Saalfeld, S., Schmid, B., et al. (2012). Fiji: an open-source platform for biological-image analysis. Nat Methods *9*, 676–682.

Shen, Y., and Bax, A. (2013). Protein backbone and sidechain torsion angles predicted from NMR chemical shifts using artificial neural networks. J. Biomol. NMR *56*, 227–241.

Silhan, J., Vacha, P., Strnadova, P., Vecer, J., Herman, P., Sulc, M., Teisinger, J., Obsilova, V., and Obsil, T. (2009). 14-3-3 protein masks the DNA binding interface of forkhead transcription factor FOXO4. J. Biol. Chem. *284*, 19349–19360.

Simon, B., Madl, T., Mackereth, C.D., Nilges, M., and Sattler, M. (2010). An efficient protocol for NMR-spectroscopy-based structure determination of protein complexes in solution. Angew. Chem. Int. Ed. Engl. *49*, 1967–1970.

Singh, A., Ye, M., Bucur, O., Zhu, S., Tanya Santos, M., Rabinovitz, I., Wei, W., Gao, D., Hahn, W.C., and Khosravi-Far, R. (2010). Protein phosphatase 2A reactivates FOXO3a through a dynamic interplay with 14-3-3 and AKT. Mol. Biol. Cell *21*, 1140–1152.

Sreekumar, A., Toneff, M.J., Toh, E., Roarty, K., Creighton, C.J., Belka, G.K., Lee, D.K., Xu, J., Chodosh, L.A., Richards, J.S., and Rosen, J.M. (2017). WNT-Mediated Regulation of FOXO1 Constitutes a Critical Axis Maintaining Pubertal Mammary Stem Cell Homeostasis. Dev. Cell *43*, 436–448.e6.

Sun, J., and Weis, W.I. (2011). Biochemical and structural characterization of β-catenin interactions with nonphosphorylated and CK2-phosphorylated Lef-1. J. Mol. Biol. *405*, 519–530.

Sunayama, J., Tsuruta, F., Masuyama, N., and Gotoh, Y. (2005). JNK antagonizes Akt-mediated survival signals by phosphorylating 14-3-3. J. Cell Biol. *170*, 295–304.

Svergun, D.I. (1992). Determination of the Regularization Parameter in Indirect-Transform Methods Using Perceptual Criteria. J Appl Crystallogr *25*, 495–503.

Tenbaum, S.P., Ordóñez-Morán, P., Puig, I., Chicote, I., Arqués, O., Landolfi, S., Fernández, Y., Herance, J.R., Gispert, J.D., Mendizabal, L., et al. (2012). β-catenin confers resistance to PI3K and AKT inhibitors and subverts FOXO3a to promote metastasis in colon cancer. Nat. Med. *18*, 892–901.

Theillet, F.X., Rose, H.M., Liokatis, S., Binolfi, A., Thongwichian, R., Stuiver, M., and Selenko, P. (2013). Site-specific NMR mapping and time-resolved monitoring of serine and threonine phosphorylation in reconstituted kinase reactions and mammalian cell extracts. Nat. Protoc. *8*, 1416–1432.

Theillet, F.X., Binolfi, A., Frembgen-Kesner, T., Hingorani, K., Sarkar, M., Kyne, C., Li, C., Crowley, P.B., Gierasch, L., Pielak, G.J., et al. (2014). Physicochemical properties of cells and their effects on intrinsically disordered proteins (IDPs). Chem. Rev. *114*, 6661–6714.

Tompa, P. (2012). Intrinsically disordered proteins: a 10-year recap. Trends Biochem. Sci. *37*, 509–516.

Tsai, K.L., Sun, Y.J., Huang, C.Y., Yang, J.Y., Hung, M.C., and Hsiao, C.D. (2007). Crystal structure of the human FOXO3a-DBD/DNA complex suggests the effects of post-translational modification. Nucleic Acids Res. *35*, 6984–6994.

Tzivion, G., Dobson, M., and Ramakrishnan, G. (2011). FoxO transcription factors; regulation by AKT and 14-3-3 proteins. Biochim. Biophys. Acta *1813*, 1938–1945.

Uversky, V.N., Davé, V., Iakoucheva, L.M., Malaney, P., Metallo, S.J., Pathak, R.R., and Joerger, A.C. (2014). Pathological unfoldomics of uncontrolled chaos: intrinsically disordered proteins and human diseases. Chem. Rev. *114*, 6844–6879.

Valenta, T., Hausmann, G., and Basler, K. (2012). The many faces and functions of β-catenin. EMBO J. *31*, 2714–2736.

van der Horst, A., and Burgering, B.M.T. (2007). Stressing the role of FoxO proteins in lifespan and disease. Nat. Rev. Mol. Cell Biol. *8*, 440–450.

van der Lee, R., Buljan, M., Lang, B., Weatheritt, R.J., Daughdrill, G.W., Dunker, A.K., Fuxreiter, M., Gough, J., Gsponer, J., Jones, D.T., et al. (2014). Classification of intrinsically disordered regions and proteins. Chem. Rev. *114*, 6589–6631.

van der Vos, K.E., and Coffer, P.J. (2008). FOXO-binding partners: it takes two to tango. Oncogene *27*, 2289–2299.

van Dongen, E.M., Evers, T.H., Dekkers, L.M., Meijer, E.W., Klomp, L.W., and Merkx, M. (2007). Variation of linker length in ratiometric fluorescent sensor proteins allows rational tuning of Zn(II) affinity in the picomolar to femtomolar range. J. Am. Chem. Soc. *129*, 3494–3495.

Vranken, W.F., Boucher, W., Stevens, T.J., Fogh, R.H., Pajon, A., Llinas, M., Ulrich, E.L., Markley, J.L., Ionides, J., and Laue, E.D. (2005). The CCPN data model for NMR spectroscopy: development of a software pipeline. Proteins *59*, 687–696.

Vuzman, D., Azia, A., and Levy, Y. (2010). Searching DNA via a "Monkey Bar" mechanism: the significance of disordered tails. J. Mol. Biol. *396*, 674–684.

Wang, F., Marshall, C.B., Yamamoto, K., Li, G.Y., Plevin, M.J., You, H., Mak, T.W., and Ikura, M. (2008). Biochemical and structural characterization of an intramolecular interaction in FOXO3a and its binding with p53. J. Mol. Biol. *384*, 590–603.

Wang, F., Marshall, C.B., Yamamoto, K., Li, G.Y., Gasmi-Seabrook, G.M., Okada, H., Mak, T.W., and Ikura, M. (2012). Structures of KIX domain of CBP in complex with two FOXO3a transactivation domains reveal promiscuity and plasticity in coactivator recruitment. Proc. Natl. Acad. Sci. USA *109*, 6078–6083.

Weigel, D., and Jäckle, H. (1990). The fork head domain: a novel DNA binding motif of eukaryotic transcription factors? Cell *63*, 455–456.

Wiśniewski, J.R., Zougman, A., Nagaraj, N., and Mann, M. (2009). Universal sample preparation method for proteome analysis. Nat. Methods *6*, 359–362.

Wouters, F.S., Bastiaens, P.I., Wirtz, K.W., and Jovin, T.M. (1998). FRET microscopy demonstrates molecular association of non-specific lipid transfer protein (nsL-TP) with fatty acid oxidation enzymes in peroxisomes. EMBO J. *17*, 7179–7189.

Wright, P.E., and Dyson, H.J. (2015). Intrinsically disordered proteins in cellular signalling and regulation. Nat. Rev. Mol. Cell Biol. *16*, 18–29.

Xing, Y., Clements, W.K., Kimelman, D., and Xu, W. (2003). Crystal structure of a beta-catenin/axin complex suggests a mechanism for the beta-catenin destruction complex. Genes Dev. *17*, 2753–2764.

Yang, S., Liu, Y., Li, M.Y., Ng, C.S.H., Yang, S.L., Wang, S., Zou, C., Dong, Y., Du, J., Long, X., et al. (2017). FOXP3 promotes tumor growth and metastasis by activating Wnt/β-catenin signaling pathway and EMT in non-small cell lung cancer. Mol. Cancer *16*, 124.

Zamudio, A.V., Dall'Agnese, A., Henninger, J.E., Manteiga, J.C., Afeyan, L.K., Hannett, N.M., Coffey, E.L., Li, C.H., Oksuz, O., Sabari, B.R., et al. (2019). Mediator Condensates Localize Signaling Factors to Key Cell Identity Genes. Mol. Cell *76*, 753–766.e6.

Zhang, N., Wei, P., Gong, A., Chiu, W.T., Lee, H.T., Colman, H., Huang, H., Xue, J., Liu, M., Wang, Y., et al. (2011). FoxM1 promotes β-catenin nuclear localization and controls Wnt target-gene expression and glioma tumorigenesis. Cancer Cell *20*, 427–442.

Zhao, Y., Yang, J., Liao, W., Liu, X., Zhang, H., Wang, S., Wang, D., Feng, J., Yu, L., and Zhu, W.G. (2010). Cytosolic FoxO1 is essential for the induction of autophagy and tumour suppressor activity. Nat. Cell Biol. *12*, 665–675.

STAR★METHODS

KEY RESOURCES TABLE

REAGENT or RESOURCE	SOURCE	IDENTIFIER
Antibodies		
Anti-HA(12CA5)	Home made	N/A
Anti-Myc(9E10)	Home made	N/A
Anti-FLAG M2	Sigma	Cat#F1804; RRID: AB_262044
phospho T32 FOXO4	Abcam	Cat#ab128876; RRID: AB_11140855
phospho S193 FOXO4	Abcam	Cat#ab174849
phospho S262 FOXO4	Abcam	Cat#ab126594; RRID: AB_11130059
phosphor S473 AKT/PKB	Cell Signaling Technology	Cat#4060; RRID: AB_2315049
anti-14-3-3beta	Santa Cruz Biotechnology	Cat#SC-629; RRID: AB_2273154
anti-β-catenin	BD Biosciences	Cat#610154; RRID: AB_397555
anti-HA beads	Sigma	Cat#A2095; RRID: AB_257974
Anti-FLAG M2 beads	Sigma	Cat#A2220; RRID: AB_10063035
Strep-tactin beads	IBA	Cat#2-4030-002
GFP-TrapA beads	Chromotek	Cat#gta-20; RRID: AB_2631357
Bacterial and virus strains		
BL21-(DE3) Star	Invitrogen	Cat#601003
Chemicals, peptides, and recombinant proteins		
hydrogen peroxide (H_2O_2)	Sigma	Cat#216763; CAS: 7722-84-1
Okadaic Acid	Merck chemicals	Cat#495604; CAS: 78111-17-8
PKB inhibitor VIII	Santa Cruz Biotechnology	Cat#SC-202048A; CAS: 612847-09-3
WNT-C59	Bio-Techne	Cat#5148; CAS: 1243243-89-1
Ni-NTA agarose	QIAGEN	Cat#30250
3-(2-Iodoacetamido)-PROXYL	Sigma	Cat#253421
complete protease inhibitor cocktail	Roche	Cat#11697498001
phosphatase inhibitor cocktail	Roche	Cat#4906845001
AKT/PKB	Millipore	Cat#14-276
CK1	Millipore	Cat#14-520
Biotin-FOXO4$^{CR\text{-}PKB/AKT}$ (residues 240-280)	Peptide Specialty Laboratories GmbH	N/A
Biotin-FOXO4^{CR3} (residues 464-500)		N/A
Biotin-FOXO4 (residues 252-281)	Home made Home made	N/A
Biotin-FOXO4-pSer262 (residues 252-281)		N/A
PP2A purified	Merck chemicals	Cat#14-111
FOXO4^{C} (residues 200-505)	This paper	N/A
FOXO4$^{CR\text{-}PKB/AKT}$ (residues 240-280)	This paper	N/A
FOXO4^{CR3} (residues 462-500)	This paper	N/A
FOXO4^{N} (residues 1-80)	This paper	N/A
FOXO4^{FH} (residues 86-207)	This paper	N/A
FOXO4^{FH+CR3} (residues 86-201 plus 458-505)	This paper	N/A
FOXO4$^{FH\Delta N}$ (residues 105-207)	This paper	N/A
β-catenin (residues 1-781)	This paper	N/A
β-catenin^{ARMN} (residues 141-305)	This paper	N/A
LEF-1 (residues 1-101)	This paper	N/A
Axin-1 (residues 351-500)	This paper	N/A
ICAT (residues 1-81)	This paper	N/A

(*Continued on next page*)

Continued

REAGENT or RESOURCE	SOURCE	IDENTIFIER
Critical commercial assays		
Dual-Luciferase® Reporter Assay System	Promega	Cat#E1910
micro BCA protein assay kit	ThermoFisher Scientific	Cat#23235
Deposited data		
$FOXO4^{CR\text{-}PKB/AKT}$	Biological Magnetic Resonance Data Bank	50401
$FOXO4^{CR3}$	Biological Magnetic Resonance Data Bank	50402
$FOXO4^{FH}$	Biological Magnetic Resonance Data Bank	50398
$FOXO4^{FH+CR3}$	Biological Magnetic Resonance Data Bank	50403
Mass spectrometry proteomics data	ProteomeXchange Consortium (PRIDE partner)	PXD026263
Experimental models: cell lines		
HEK293T	ATCC	CRL-11268; RRID: CVCL_0063
U2OS	ATCC	HTB-96; RRID: CVCL_0042
DLD1	ATCC	CCL-221; RRID: CVCL_0248
Oligonucleotides		
CTDSP2 response element 1 DNA sense: CCAGATAAACAACCCG	Eurofins MWG Operon	N/A
CTDSP2 response element 1 DNA antisense: CGGGTTGTTTATCTGG	Eurofins MWG Operon	N/A
Recombinant DNA		
CFP-FOXO-YFP YFP-FOXO4-YFP CFP-FOXO4-CFP YFP-FOXO4-CFP	This paper This paper This paper This paper	N/A N/A N/A N/A
HA-FOXO4	Kops et al., 1999	N/A
HA-FOXO4 DC HA-FOXO4 DC2 HA-FOXO4 DN	This paper This paper This paper	N/A N/A N/A
CFP-T28AFOXO4-YFP CFP-T28ASER193AFOXO4-YFP HA-TCF4 Flag-ICAT Flag-β-catenin	This paper This paper Hoogenboom et al., 2008 This paper Essers et al., 2005	N/A N/A N/A N/A N/A
pETM11-His6-ZZ-tev- $FOXO4^{C}$	This paper	N/A
pETM11-His6-ZZ-tev- $FOXO4^{CR\text{-}PKB/AKT}$	This paper	N/A
pETM11-His6-ZZ-tev- $FOXO4^{CR3}$	This paper	N/A
pETM11-His6-ZZ-tev- $FOXO4^{N}$	This paper	N/A
pETM11-His6-ZZ-tev- $FOXO4^{FH}$	This paper	N/A
pETM11-His6-ZZ-tev- $FOXO4^{FH+CR3}$	This paper	N/A
pETM11-His6-ZZ-tev- $FOXO4^{FH\Delta N}$	This paper	N/A
pETM11-His6-ZZ-tev- β-catenin	This paper	N/A
pETM11-His6-ZZ-tev- $\beta\text{-catenin}^{ARMN}$	This paper	N/A
pETM11-His6-ZZ-tev- LEF-1	This paper	N/A
pETM11-His6-ZZ-tev- Axin-1	This paper	N/A
pETM11-His6-ZZ-tev- ICAT	This paper	N/A
Software and algorithms		
GraphPad	GraphPad	https://www.graphpad.com
ImageJ	Schindelin et al., 2012	https://imagej.net
Multimodal FRET analysis macro	Ponsioen et al., 2021	N/A
Ccpnmr 2.4	Vranken et al., 2005	N/A
TOPSPIN 3.0	Bruker	N/A
CNS	Brünger et al., 1998; Linge et al., 2003; Nilges, 1995; Simon et al., 2010	N/A
TALOS-N	Shen and Bax, 2013	N/A

(*Continued on next page*)

Continued

REAGENT or RESOURCE	SOURCE	IDENTIFIER
PyMOL Molecular Graphics System, Version 2.4	Schrödinger, LLC	N/A
GIFT	PCG-Software	N/A
SAXSQuant 3.9	Anton-Paar	N/A
GNOM	Svergun, 1992	N/A
ATSAS 2.5 package	EMBL	N/A
EOM	Bernadó et al., 2007	N/A
SEDVIEW	Hayes and Stafford, 2010	N/A

RESOURCE AVAILABILITY

Lead contact

Further information and requests for resources and reagents should be directed to and will be fulfilled by Tobias Madl: tobias.madl@medunigraz.at.

Materials availability

All materials and construct used in this study are available upon request. Transfer may require completion of material transfer agreement. Commercially available reagents are indicated in the Key resources table.

Data and code availability

The mass spectrometry proteomics data and NMR chemical shifts assignment have been deposited at the ProteomeXchange Consortium via the PRIDE partner repository (https://www.ebi.ac.uk/pride) and at the Biological Magnetic Resonance Bank, respectively and are publicly available as of the date of publication. Accession numbers are listed in the Key resources table.

All data reported in this paper will be shared by the lead contact upon request.

This study does not report original code.

Any additional information required to reanalyze the data reported in this paper is available from the lead contact upon request.

EXPERIMENTAL MODEL AND SUBJECT DETAILS

U2OS Human Bone Osteosarcoma cells (female origin) and 293T Human Embrionic Kidney cells (HEK293T, fetal origin) were obtained from the ATCC and cultured at 37°C and 5% CO_2 in DMEM supplemented with 100U/ml penicillin (Lonza), 100mg/ml streptomycin (Lonza) and 10% FBS (Lonza). DLD1 Human Colorectal Adenocarcinoma cells(Kops et al., 2002) were obtained from the ATCC and cultured at 37°C and 5% CO_2 in RPMI-1640 medium with 100U/ml penicillin, 100mg/ml streptomycin (Lonza) and 10% FBS (Lonza).

METHOD DETAILS

Constructs and transfections

Expression constructs for the fragments of human FOXO4 (Uniprot ID P98177) from amino acid 200 to 505 ($FOXO4^{C}$), amino acid 1 to 80 ($FOXO4^{N}$), amino acid 86 to 207 ($FOXO4^{FH}$), amino acid 105 to 207 ($FOXO4^{FH\Delta N}$) amino acid 86 to 201 plus 458 to 505 ($FOXO4^{FH+CR3}$), amino acid 240 to 280 ($FOXO4^{CR\text{-}PKB/AKT}$) and amino acid 462 to 500 ($FOXO4^{CR3}$) were generated by synthesis of the corresponding optimized FOXO4 cDNA constructs (Genscript) and insertion of these cDNA into a pETM11-ZZ-His_6 vector via NcoI/BamHI restriction digest. We also generated optimized cDNA expression constructs (Genscript) in a pETM11-ZZ-His_6 vector corresponding to cysteine mutants of the $FOXO4^{FH}$ construct (D140C, N145C, S162C and N181C) and $FOXO4^{FH+CR3}$ construct (S116C, C481S). We also generated optimized cDNA expression constructs (Genscript) in a pETM11-ZZ-His_6 vector for human β-catenin (Uniprot ID P35222) from amino acids 1 to 781 (β-catenin) and from amino acids 141 to 305 ($\beta\text{-catenin}^{ARMN}$). We also generated optimized cDNA expression constructs (Genscript) in a pETM11-ZZ-His_6 vector for human LEF-1 (Uniprot ID Q9UJU2) from amino acids 1 to 101 (LEF-1) and Axin-1 (Uniprot ID O15169) from amino acids 351 to 500 (Axin-1) and ICAT (Uniprot ID Q9NSA3) from amino acids 1 to 81 (ICAT)

HA-FOXO4, flag-β-catenin were previously described (Essers et al., 2004). To construct a mammalian expression vector for flag-tagged ICAT/CTNNBIP1, RNA was isolated from 293T cells and used to generate cDNA. Next ICAT cDNA was obtained by PCR using as reverse primer: GGGGACCACTTTGTACAAGAAAGCTGGGTCTACTGCCTCCGGTCTTCCG; forward primer: GGGG ACAAGTTTGTACAAAAAAGCAGGCTTGATGAACCGCGAGGGAGCTC. The PCR product was cloned into the gateway vector PDon201, to generate the ICAT entry clone which was used for further cloning into destination vectors.

FRET probes pCDNA3-CFP-FOXO4-YFP, pCDNA3-YFP-FOXO4-CFP, pCDNA3-CFP-FOXO4-CFP and pCDNA3-YFP-FOXO4-YFP. CFP, FOXO4 and YFP were assembled in the pCDNA3 backbone plasmid through Gibson assembly cloning. The strategy was applied to FOXO4-Δ91-104, FOXO4-T32A and FOXO4-T32A/S193A mutant FOXO4 FRET constructs.

HEK293T and U2OS cells were transiently transfected using X-tremegene 9 reagent according to manufacturer (Roche). DLD1 cells were transiently transfected using Fugene 6 reagent according to manufacturer (Promega).

Protein expression and purification

For expression of recombinant unlabeled or ^{15}N labeled or ^{15}N-^{13}C labeled ZZ- His_6 proteins, the bacterial expression vectors were transformed into *Eschericia Coli* BL21-DE3 Star strain and 1 L expression cultures were grown for 2 days in minimal medium supplemented with either 6 g of $^{12}C_6H_{12}O_6$ or 2 g of $^{13}C_6H_{12}O_6$ (Cambridge Isotope Laboratories) and either 3 g of $^{14}NH_4Cl$ or 1 g of $^{15}NH_4Cl$ (Sigma). Cells were diluted to an OD (600nm) of 0,8 and induced with 0.5 mM IPTG followed by protein expression 16 h at 20°C. Cells pellets corresponding for protein expression of unlabeled or ^{15}N labeled or ^{15}N-^{13}C labeled disordered proteins fragments ($FOXO4^{C}$, $FOXO4^{CR\text{-}PKB/AKT}$, $FOXO4^{CR3}$, $FOXO4^{N}$, LEF-1 and Axin-1) were harvested and sonicated in denaturing lysis buffer (50 mM Tris-HCl pH 7.5, 150 mM NaCl, 20 mM Imidazole, 6 M urea) whereas the folded proteins fragments ($FOXO4^{FH}$ and cysteine mutants, $FOXO4^{FH+CR3}$ and cysteine mutant, $FOXO4^{FH\Delta N}$, ICAT, β-$catenin^{ARMN}$ and β-catenin) were harvested and sonicated in non-denaturating lysis buffer (50 mM Tris-HCl pH 7.5, 150 mM NaCl, 20 mM Imidazole, 2 mM tris(2-carboxyethyl)phosphine). ZZ-His_6 recombinant proteins were then purified using Ni-NTA agarose (QIAGEN) and the ZZ-His6 tag was cleaved with TEV protease treatment. Untagged proteins were then isolated performing a second affinity purification using Ni-NTA beads. A final size exclusion chromatography purification step was performed in the buffer of interest on a gel filtration column (Superdex 200, GE Healthcare for β-catenin, Superdex 75, GE Healthcare for $FOXO4^{FH}$ and cysteine mutants, $FOXO4^{FH\Delta N}$, $FOXO4^{FH+CR3}$ and cysteine mutant, $FOXO4^{C}$, $FOXO4^{N}$, β-$catenin^{ARMN}$, LEF-1, ICAT, Axin-1 and Superdex peptide, GE Healthcare for $FOXO4^{CR\text{-}PKB/AKT}$, $FOXO4^{CR3}$). Protein concentrations were estimated based on their absorbance at 280 nm, assuming that the ε at 280 nm was equal to the theoretical ε value.

Paramagnetic labeling

We designed several single cysteine versions of the $FOXO4^{FH}$, $FOXO4^{CR3}$ and $FOXO4^{FH+CR3}$ constructs where the cysteine has been introduced in position 140, 145, 162 and 181 ($FOXO4^{FH}$) or in position 488 ($FOXO4^{CR3}$) or 116 and 481 ($FOXO4^{FH+CR3}$). The $FOXO4^{FH}$ and $FOXO4^{FH+CR3}$ cysteine mutants have been expressed and purified according to the corresponding method sections. $FOXO4^{FH}$ and $FOXO4^{FH+CR3}$ mutated constructs were then incubated 30 minutes in presence of 5mM DTT followed by buffer exchange in 1M Tris-HCl (pH 8). 50μM of the $FOXO4^{FH}$ and $FOXO4^{FH+CR3}$ constructs were then incubated 16 hours at 4°C in presence of 8 times excess of the paramagnetic 3-(2-Iodoacetamido)-PROXYL tag. The excess of tag was removed using a final gel filtration step (Superdex 75, GE Healthcare) in a buffer containing 50mM Tris-HCl (pH 7.5), 150mM NaCl and 2mM tris(2-carboxyethyl)phosphine. The paramagnetic 3-(2-Iodoacetamido)-PROXYL tagged $FOXO4^{CR3}$ mutated constructs were purchased from Peptide Specialty Laboratories GmbH (Heidelberg, German) and dissolved in a buffer containing 50mM Tris-HCl (pH 7.5), 150mM NaCl and 2mM tris(2-carboxyethyl)phosphine.

Oligos

CTDSP2 response element 1 DNA (sense: CCAGATAAACAACCCG, antisense: CGGGTTGTTTATCTGG) were purchased from Eurofins MWG Operon. DNA duplexes were formed by mixing equimolar amounts of sense and antisense strands in H_2O, heating the mixture to 95°C for 10 minutes and slowly cooling to 4°C overnight.

Peptides

Biotin-$FOXO4^{CR\text{-}PKB/AKT}$ (residues 240-280) and biotin-$FOXO4^{CR3}$ (residues 464-500) with an N-terminal biotin were purchased from Peptide Specialty Laboratories GmbH (Heidelberg, German). Biotin-$FOXO4^{CR\text{-}PKB/AKT}$ (residues 252-281) and biotin- pSer262-FOXO4 (residues 252-281, phosphorylated at 262) with an N-terminal biotin and a double glycine linker were self-synthesized.

Isothermal titration calorimetry (ITC)

All proteins and DNA samples were equilibrated either in buffer containing 50mM Tris-HCl (pH 7.5), 150mM NaCl and 2mM tris(2-carboxyethyl)phosphine (Figures S3A–S3C and S3F) or in buffer containing 20mM HEPES (pH 7.0), 50mM NaCl, 5mM DTT (Figures S3D and S3E). ITC measurements were taken with a MicroCal VP-ITC instrument (Microcal, Northhampton, USA) with either 28 rounds of 10 μL injections at 10°C (Figures S3A–S3C and S3F) or 18 rounds of 15 μl injections at 25°C (Figures S3D and S3E). Integration of peaks corresponding to each injection, subtraction of the contribution of protein dilution, correction for the baseline and curve fitting were performed using the MicroCal VP-ITC analysis software provided by the manufacturer. Curve fitting was done using standard one-site model and gives the equilibrium binding constant (*Ka*), the stoichiometry (n) and enthalpy of the complex formation (ΔH).

Estimation of the effective molarity

The distribution function describing the probability ($\boldsymbol{P}(\boldsymbol{r_e})$) of a certain end-to-end distance ($\boldsymbol{r_e}$) for the linker between the FOXO4 FH domain and the CR3 region was calculated using a worm-like chain model assuming a persistence length ($\boldsymbol{l_p}$) of 4.5 $\boldsymbol{\AA}$. according to

the below equation (van Dongen et al., 2007). In this equation the total contour length l_c is equal to $b_0 n$, where n is the number of peptide bonds in the linker (280) and b_0 is the average distance between adjacent Cα atoms, 3.8 Å.

$$P(r_e) = 4\pi r_e^2 (3/4\pi l_p l_c)^{\frac{3}{2}} \exp\left(-\frac{3r_e^2}{4l_p l_c}\right)\left(1 - \frac{5l_p}{4l_c} - \frac{2r_e^2}{l_c^2} + \frac{33r_e^4}{80l_p l_c^3} + \frac{79l_p^2}{160l_c^2} + \frac{329r_e^2 l_p}{120l_c^3} - \frac{6799r_e^4}{1600l_c^4} + \frac{3441r_e^6}{2800l_p l_c^5} - \frac{1089r_e^8}{12800l_p^2 l_c^6}\right)$$

The effective concentration for the formation of a complex is proportional to the probability density ($p(r_e)$) for the end-to-end distance (r_e) that the linker needs to bridge in the complex, which is given by:

$$p(r_e) = P(r_e)/4\pi r_e^2$$

When r_e, l_c, and l_p, are given in dm, the effective concentration $C_{eff}$is obtained by dividing $p(r_e)$ by Avogadro's constant:

$$C_{eff} = p(r_e)/N_{AV}$$

NMR spectroscopy

NMR experiments were performed at 25°C (except for the FOXO4^{FH} - β-catenin titration, 10°C) on Bruker 600, 700 and 900 MHz spectrometers equipped with triple-resonance cryo-probes or on a Bruker 600 MHz Avance Neo NMR spectrometer equipped with a TXI room temperature probe. Besides the ^{1}H, ^{15}N HSQC spectrum, the following three-dimensional spectra were acquired for NMR resonance assignment of FOXO4^{C}, FOXO4$^{CR\text{-}PKB/AKT}$, FOXO4^{CR3}, FOXO4^{FH} and FOXO4^{FH+CR3}: HNCO, HN(CA)CO, HNCACB, CBCA(CO)NH, (H)CC(CO)NH-TOCSY, HNCA, HCCH-TOCSY, HN(CA)NNH and H(NCA)NNH using between 400 and 700 μM of ^{1}H, ^{15}N, ^{13}C labeled proteins and 10% D_2O. Spectra were processed using TOPSPIN 3.0 (Bruker) and analyzed using CcpNmr 2.4. (Vranken et al., 2005). NMR chemical shifts have been submitted to the Biological Magnetic Resonance Bank (BMRB) under the accession numbers BMRB 50401 (FOXO4$^{CR\text{-}PKB/AKT}$), BMRB 50402 (FOXO4^{CR3}), BMRB 50398 (FOXO4^{FH}) and BMRB 50403 (FOXO4^{FH+CR3}).

For the NMR binding assays, all protein samples were equilibrated in the same buffer containing 50 mM Tris-HCl (pH 7.5), 150 mM NaCl and 2 mM tris(2-carboxyethyl)phosphine. ^{1}H, ^{15}N HSQC experiments were recorded according to the NMR section. The CSPs was calculated according to the following equation: $CSP_{1H15N} = ((\Delta\delta H)^2/2 + (\Delta\delta N/10)^2/2)^{1/2}$, where ΔδH and ΔδN indicate the chemical shift changes of the amide proton and nitrogen, respectively, using CcpNMR 2.4 (Vranken et al., 2005) . The intensity ratio (I_{bound}/I_{free}) corresponds to the intensity ratio of the ^{1}H, ^{15}N HSQC labeled construct cross-peaks in the ligand bound and free forms. The unassigned residues are indicated in gray in the corresponding CSP and intensity ratio bar-plots presented in Figures 1C–1F, 2C, 3C, and 3E.

To obtain inter-molecular NOE-based distance restraints, we generated asymmetrically labeled samples. To this end, two complexes were generated: i) ^{1}H, ^{15}N, ^{13}C labeled FOXO4^{FH} at 500 μM in complex with 700 μM of unlabeled FOXO4^{CR3} and ii) ^{1}H, ^{15}N, ^{13}C labeled FOXO4^{CR3} at 500 μM in complex with 700 μM of unlabeled FOXO4^{FH}, in a buffer containing 50 mM Tris-HCl (pH 7.5), 150 mM NaCl and 2 mM tris(2-carboxyethyl)phosphine. ^{1}H,^{13}C,^{15}N filtered, ^{13}C- edited NOESY-HSQC and ^{1}H,^{13}C edited NOESY-HSQC spectra were recorded to obtain and to discriminate between inter-and intra-molecular NOEs, respectively.

Structure determination

Due to intermediate exchange only a few inter-molecular NOEs (48) could be obtained. To obtain additional restraints for structure determination, we determined paramagnetic relaxation enhancements (PREs) for a set of 5 complexes *in trans* configuration and 2 complexes *in cis* configuration containing spin-labeled (SL) samples (*in trans*: SL-FOXO4^{FH}-D140C/ FOXO^{CR3} ; SL-FOXO4^{FH}-D145C/ FOXO^{CR3} ; SL-FOXO4^{FH}-S162C/FOXO^{CR3}; SL-FOXO4^{FH}-N181C/FOXO^{CR3}; SL-FOXO4^{CR3}-C481S&S488C/FOXO^{FH}. *in cis:* SL-FOXO4^{FH+CR3} C481 and SL-FOXO4^{FH+CR3} C481S&S116C) (Figures S4A–S4G). In all of the complexes *in trans*, the SL component was unlabeled, and the binding partner (FOXO4^{FH} or FOXO4^{CR3}) ^{13}C,^{15}N,^{1}H labeled. ^{1}H, ^{15}N, ^{13}C labeled FOXO4^{FH} were mixed at 1:2 equivalents with SL-FOXO4^{CR3} and inversely. In the 2 complexes *in cis* the SL-FOXO4^{FH+CR3} were ^{13}C,^{15}N,^{1}H labeled. ^{1}H, ^{15}N and ^{1}H, ^{13}C HSQC spectra with long inter-scan delays (4 s) were recorded both in the paramagnetic state and the diamagnetic state at a final concentration of 100 μM of the ^{13}C/^{15}N-labeled protein. 5 mM of ascorbic acid were added to reduce the paramagnetic label and to obtain the diamagnetic reference spectra. Intensity ratios between the paramagnetic and diamagnetic state were calculated (Battiste and Wagner, 2000; Simon et al., 2010) for all assigned and non-overlapping ^{1}H, ^{15}N and ^{1}H, ^{13}C HSQC cross-peaks as described and using a correlation time of the electron-spin interaction vector of 4 ns (determined from ^{1}H-R_1, ^{1}H-R_2 data obtained for a complex sample spin labeled at position C481).

Structures were calculated using modified CNS protocols in the ARIA/CNS setup (Brünger et al., 1998; Linge et al., 2003; Nilges, 1995; Simon et al., 2010) and using the NMR-based structure of FOXO4 FH as template (PDB ID 1E17). In brief, the protocol consists of the following steps: (1) generation of flexible regions in FOXO4^{FH} (residues 86-104 and 186-207), the FOXO4^{CR3} peptide, and spin labels, randomization of the flexible regions; (2) molecular dynamics simulated annealing restraining FOXO4^{FH} (without flexible regions) harmonically to its template structure (using a non-crystallographic force constant of 10,000 kcal mol^{-1} Å^{-2}), with additional dihedral angle restraints from ^{1}H, ^{15}N and ^{13}C chemical shifts using TALOS-N (Shen and Bax, 2013), hydrogen bond restraints (regions 468-477 and 481-488; based on ^{13}C secondary chemical shifts (ΔCα-ΔCβ) (Figure S4H) and consistent formation of α-helical structure in initial rounds of structure calculations in which no hydrogen bond restraints were defined), inter-molecular PRE restraints (4 non-interacting copies of the spin label to account for different spin label orientations), and inter- and intra-molecular NOE

restraints. Simulated annealing protocols and temperature course are the same as in standard structure calculations. A total of 200 structures were calculated and the 10 lowest energy structures used to prepare the figures using the PyMOL Molecular Graphics System, Version 2.4 (Schrödinger, LLC).

Phosphorylation assays in HEK293T cell extracts

200 μl of HEK293T cell pellet was re-suspended in 400 μl of lysis buffer containing 50 mM Tris-HCl (pH 7.5), 150 mM NaCl, 1% Triton-X and 2 mM tris(2-carboxyethyl)phosphine, one tablet of complete protease inhibitor cocktail (Roche, #11697498001), and one tablet of phosphatase inhibitor cocktail (Roche, phosSTOP #4906845001). The lysate was kept on ice for 15 minutes with gentle shaking every 2 minutes, then centrifuged at 13,000 g for 10 minutes at 4°C. The total protein concentration was determined by micro BCA (Pierce, USA). ^{1}H, ^{15}N, ^{13}C labeled His_6-ZZ-$FOXO4^{CR\text{-}PKB/AKT}$ at a final concentration of 50 μM were incubated 16 hours at room temperature with 12-15 mg/ml of HEK293T cell extract in presence of 10 mM $MgCl_2$ and 10 mM ATP. Untagged $FOXO4^{CR\text{-}PKB/AKT}$ was then re-purified in a buffer containing 50 mM Tris-HCl (pH 6.5), 150 mM NaCl and 2 mM tris(2-carboxyethyl)phosphine according to the section protein expression and purification, concentrated to 500μM and NMR backbone resonance assignment was carried according to the NMR section.

In vitro, AKT and CK1 phosphorylation assays

Phosphorylation of ^{1}H,^{15}N,^{13}C labeled $FOXO4^{CR\text{-}PKB/AKT}$ by AKT (Millipore, #14-276) or CK1 (Millipore, #14-520) or AKT plus CK1 kinases was monitored by adding 12 nM (CK1) or 7 nM (AKT) of the respective kinases to a solution at 50 μM of $FOXO4^{CR\text{-}PKB/AKT}$ equilibrated in a buffer containing 50 mM Tris-HCl (pH 6.5), 150 mM NaCl, 2 mM tris(2-carboxyethyl)phosphine, 10 mM MgCl2 and 10 mM ATP. A series of ^{1}H, ^{15}N HSQCs was recorded after each other until the AKT or CK1 reaction stopped. Phosphorylated $FOXO4^{CR\text{-}PKB/AKT}$ were then concentrated to 500 μM and backbone assigned according to the NMR section.

SAXS

SAXS data for a solution of $FOXO4^{FH+CR3}$ were recorded at an in-house SAXS instrument (SAXSess mc2, Anton Paar, Graz, Austria) equipped with a Kratky camera, a sealed X-ray tube source and a one-dimensional reverse-biased silicon diode array detector (Mythen 1K, Dectris, Baden, Switzerland). Scattering patterns were measured with 30-min (3 frames, each 10 minutes) exposure times. Measurements were carried out for several solute concentrations in the range from 1 to 10 mg/ml. Radiation damage was excluded based on a comparison of individual frames of the exposures, where no changes were detected. A range of momentum transfer of $0.01 < s < 0.7$ $Å^{-1}$ was covered ($s = 4\pi \sin(\theta)/\lambda$, where 2θ is the scattering angle and $\lambda = 1.5$ Å is the X-ray wavelength). The data were processed with the SAXSQuant software (version 3.9), and desmeared using the programs GNOM (Svergun, 1992) and GIFT (PCG software). EOM analysis was performed with the ATSAS 2.5 package (EMBL, Hamburg). EOM calculations were carried out using the EOM program (Bernadó et al., 2007) and using default settings. A random pool of 100,000 independent structures was generated using the primary sequence and the available structure of $FOXO4^{FH}$. All disordered regions were randomized. Using the built-in genetic algorithm and using the default settings, a subset of a few independent structures was selected that describes the experimental SAXS best and used to prepare the figures showing R_G/D_{max} distributions.

Ultracentrifugation analysis

Fluorescent $FOXO4^{C}$ Alexa 488 conjugates, were generated using maleimide coupling chemistry. To ensure fluorescent dye incorporation away from potential β-catenin interaction sites the FOXO4 construct used contained the following point mutations: C481S, L498C. AUC experiments were performed on a Beckmann ProteomeLab XL-A analytical ultracentrifuge equipped with the TI-50 Beckamn rotor set (Beckmann) and fluorescence detector (Aviv Biomedical). Sedimentation experiments were performed for 6 hours at 42,000 rpm at 20°C. Data Analysis was performed using SEDVIEW (Hayes and Stafford, 2010). SEDVIEW only uses a subset of the scans and averages over the resulting dc/dt plots. The range was adapted to include the most meaningful range for the species studied and included the scans 85 to 120 for each measurement. The scan range between 85 and 120 was chosen so that the first species at 1 S show a nice peak in the dc/dt plot and so that a baseline of sufficient length is visible in the higher s-value range. The position of the complex peak was also considered and as the complex is at ~4.5 S, the range of the x axis was truncated to accommodate the peak at a s-value range, where no bottom artifacts are visible yet. This range then was used for all the samples within this experiment to allow best possible comparison.

Immunoprecipitation

Non-confluent cells were lysed with RIPA lysis buffer (50 mM Tris, pH 7.5, 1% Triton X-100, 0.5% deoxycholate, 10 mM EDTA, 150 mM NaCl, 50 mM NaF, 1 μg/ml leupeptin, and 0.1 μg/ml aprotinin), lysates were centrifuged for 10 min at 14,000 rpm at 4°C. Lysates were incubated for 2 hours at 4°C with anti-HA beads (Sigma), anti-Flag beads (Sigma) or biotin labeled peptides coupled to Strep-tactin beads (IBA). The immunoprecipitations were washed four times with RIPA buffer and 25 μL of 1x Laemmli sample buffer was added to the beads. Samples were subjected to SDS-PAGE and transferred to PVDF membrane (Merck). Western blot analysis was performed under standard conditions and using the indicated antibodies.

FRET

HEK293T and U2OS cells were cultured in FluoroBrite DMEM (ThermoFisher) supplemented with 100U/ml penicillin (Lonza), 100mg/ml streptomycin (Lonza) and 10% FBS (Lonza). FRET imaging was performed on an inverted Nikon T*i* microscope with a Perfect Focus System. The microscope was held at 37°C using a Microscope Cage Incubator (OkoLab). Dishes were mounted to a culture chamber for humidity and 6% CO_2. Cells were imaged in multi-position mode with a Plan Fluor 40 × oil NA 1.3 working distance 0.2 objective. The excitation filter and dichroic mirror for both CFP and YFP were 430/24 and 450LP. The emissions from both fluorophores were collected and split simultaneously using a TuCam 509nm beamsplitter (Semrock). Then CFP emission was filtered by 483/32 filter (Semrock), YFP emission was filtered by 515LP filter (Semrock). Filtered emissions were detected separately by two Luca-EM-R-604 EMCCD cameras (Andor), controlled by company acquisition software (NIS Elements). Images were taken every 3 min for in total 90 min. H_2O_2, VIII or insulin/EGF were added to the cells during the interval between frame 5 and frame 6 (12min to 15min). Acquired images were analyzed using ImageJ macro script offered by Bas Ponsioen. The calculated CFP/YFP ratio was quantified and plotted using GraphPad Prism 8.

FRET validation by photobleaching

FRET efficiency was validated by the acceptor photobleaching methods as described previously by Wouters et al. (1998) . Images were captured with a Zeiss LSM510 microscope with a Plan-Neofluar 40x/1.30 Oil objective. U2OS cells transfected with FRET probes were fixed in 4% PFA for 10 min. A pre-photobleach CFP (donor) image of intracellular region of interest (ROI) was acquired as pre-bleach CFP intensity, by scanning with 405 nm laser. At the same ROI, YFP (acceptor) was repeated scanned with the 515 nm laser until all YFP was photodestructed. Then a second post-photobleach CFP image was acquired as post-bleach CFP intensity, by scanning with a 405 nm laser. The FRET efficiencies (%) in the ROI were calculated from two (pre-photobleach and post-photobleach) CFP images according to the formula:

$$\mathrm{FRETefficiency}(\%) = \frac{\mathrm{post} - \mathrm{photobleachintensity} - \mathrm{pre} - \mathrm{photobleachintensity}\ X100}{\mathrm{post} - \mathrm{photobleachintensity}}$$

Dual luciferase assay

For FOXO4 luciferase assay, cells were transfected with 6xDBE, CMV-Renilla, pBluescript and FOXO4 constructs. Luciferase activity was analyzed using a luminometer (TriStar^2 LB 942 multimode reader, Berthold) and a luciferase assay kit according to the manufacturer (Dual-Luciferase® Reporter Assay System, Promega). 6xDBE luciferase activity was normalized by Renilla. Results were analyzed and plotted using Excel and GraphPad Prism 8.

For TOP/FOP assay, cells were transfected with either a luciferase reporter construct bearing multiple copies of an optimal TCF-binding site (pTOPglow) or a luciferase reporter construct bearing multiple copies of a mutant form of the optimal TCF-binding site (pFOPglow), together with CMV-Renilla. Luciferase activity was analyzed using a luminometer and a dual-luciferase assay kit according to the manufacturer's protocol (Dual-Luciferase® Reporter Assay System, Promega). TCF Optimal Promoter (TOP) and Fake Optimal Promoter (FOP) luciferase activity was normalized by Renilla. Then TOP/FOP ratio was calculated by dividing normalized TOP luciferase to normalized FOP luciferase. Results were analyzed and plotted using Excel and GraphPad Prism 8.

SILAC labeling

HEK293T cells were cultured in SILAC Dulbecco's Modified Eagle Medium without arginine, lysine and glutamine (PAA, E15-086), supplemented with 1% L-Glutamine, Penicillin/Streptomycin, 10% dialized FBS (GIBCO), 73 mg/ml L-Lysine (light/K^0 (Sigma, A6969) or heavy/K^8 (Sigma, 608041 or Silantes, 211603902)) and 29.4 mg/ml arginine light/R^0 (Sigma, A6969) or heavy/R10 (Sigma, 608033 or Silantes, 201603902)). Cells were cultured in SILAC medium until labeling efficiency exceeded 95%. Labeled cells were transfected with FOXO4-GFP of co-transfected with flag-b-catenin and FOXO4-GFP. Cells were then treated with H_2O_2 (100 mM, 60 minutes) to induce b-catenin FOXO4 complex formation and harvested in lysis buffer (50 mM Tris-HCl, 1% Triton TX-100, 1.5 mM $MgCl_2$, 300 mM NaCl, 1 mM DTT and protease and phosphatase inhibitor cocktail). GFP-pulldowns were performed with GFP-TrapA beads (gta-20, Chromotek) in lysis buffer. Proteins were eluted from the GFP-beads with 0.1 M Glycine pH 2.5 and subsequently trypsinized on FASP columns (30 kDa columns). The FASP procedure is performed as described previously (Wiśniewski et al., 2009).

Mass spectrometry

Precipitated proteins were denatured with 8 M Urea in 1 M Ammonium bicarbonate (ABC) reduced with TCEP (10 mM) at room temperature for 30 minutes after which the cysteines were alkylated with Chloroacetamide (40 mM end concentration) for 30 minutes. After four-fold dilution with ABC, proteins were on-bead digested overnight at room temperature with 150 ng of Trypsin/LysC (Promega), after which peptides were bound to an in house made c18 material stage tip washed with buffer A (0.1% Formic Acid (FA)) and stored at 4°C until LC/MS-MS analysis.

LC-MS/MS and data analysis

After elution from the stage tips with buffer B (80% acetonitrile 0.1% FA), acetonitrile was removed from the samples using a SpeedVac and the remaining peptide solution was diluted with buffer A before loading. Peptides were separated on a 30 cm pico-tip column (75 μm ID, New Objective) in-house packed with 3 μm aquapur gold C-18 material (dr. Maisch) using a 140 minute gradient (7% to 80% acetonitrile 0.1% FA), delivered by an easy-nLC 1000 (Thermo), and electro-sprayed directly into a LTQ-Verlos-Orbitrap (Thermo Scientific) and analyzed in data-dependent mode with the resolution of the full scan set at 60,000, after which the top 10 peaks were selected for collision-dissociation (CID) fragmentation in the Iontrap with a target setting of 5000 ions.

Raw files were analyzed with the Maxquant software version 1.3.0.5 with deamidation of glutamine and asparagine as well as oxidation of methionine set as variable modifications, and carbamidomethylation of cysteine set as fixed modification. The Human protein database of Uniprot was searched with both the peptide as well as the protein false discovery rate set to 1%. The LFQ algorithm was used in combination with the 'match between runs' tool (option set at two minutes). Proteins identified with two or more unique peptides were filtered for reverse hits induced and standard contaminants. LFQ intensities, were log2 transformed after which identified proteins were filtered for at least three valid values in a group and missing values were replaced by imputation. After a standard t test in Perseus, p values were plotted against the difference of the mean log2 transformed LFQ values using the program R. The mass spectrometry proteomics data will be deposited at acceptance to the ProteomeXchange Consortium via the PRIDE partner repository (https://www.ebi.ac.uk/pride) with the dataset identifiers.

QUANTIFICATION AND STATISTICAL ANALYSIS

All western blot, luciferase assay and cell imaging experiments were performed with technical and biological duplicates or triplicates. Biological replicate sample sizes (n = x) and other experiment-specific details are indicated in the figure legends. Data were plotted and analyzed using GraphPad. Data are represented as the mean of multiple replicates ± SD or SEM. Figures 5B, 5G (YFP/CFP ratio change), and S5F statistical significance was determined by multiple unpaired two-tailed t tests; Figure S5G by paired two-tailed t test; Figures 5C and 5E by One-way ANOVA (Dunnett's multiple comparisons test); Figures 5G (basal FRET comparison) and S5B by One-way ANOVA (Tukey's multiple comparisons test); Figures 5F and 6E by Two-way ANOVA (Tukey's multiple comparisons test). In all analysis, differences were considered significant at $p < 0.05$ = *, $p < 0.01$ = **, $p < 0.001$ = ***, $p < 0.0001$ = ****.